Transcriptional Cartography Integrates Multiscale Biology of the Human Cortex

Authors:

Konrad Wagstyl[1*], Sophie Adler[2], Jakob Seidlitz[3,4], Simon Vandekar[5], Travis T. Mallard[6,7], Richard Dear[8], Alex R. DeCasien[9], Theodore D. Satterthwaite[3,10], Siyuan Liu[9], Petra E. Vértes[8], Russell T. Shinohara[11], Aaron Alexander-Bloch[3,4], Daniel H. Geschwind[12], Armin Raznahan[9]

1. Wellcome Centre for Human Neuroimaging, University College London, London, UK
2. UCL Great Ormond Street Institute for Child Health, 30 Guilford St, Holborn, London WC1N 1EH
3. Department of Psychiatry, University of Pennsylvania, Philadelphia, PA 19104
4. Department of Child and Adolescent Psychiatry and Behavioral Science, The Children's Hospital of Philadelphia, Philadelphia, PA 19104
5. Department of Biostatistics, Vanderbilt University, Nashville, Tennessee, USA
6. Psychiatric and Neurodevelopmental Genetics Unit, Center for Genomic Medicine, Massachusetts General Hospital, Boston, MA, USA
7. Department of Psychiatry, Harvard Medical School, Boston, MA, USA
8. Department of Psychiatry, University of Cambridge, Cambridge, CB2 0SZ, UK
9. Section on Developmental Neurogenomics, Human Genetics Branch, National Institute of Mental Health, Bethesda, MD, USA
10. Lifespan Informatics and Neuroimaging Center, University of Pennsylvania School of Medicine, Philadelphia, PA, 19104
11. Penn Statistics in Imaging and Visualization Center, Department of Biostatistics, Epidemiology, and Informatics, Perelman School of Medicine, University of Pennsylvania, Philadelphia, PA, USA
12. Center for Autism Research and Treatment, Semel Institute, Program in Neurogenetics, Department of Neurology, and Department of Human Genetics, David Geffen School of Medicine, University of California Los Angeles, Los Angeles, CA, US

Abstract

The human cerebral cortex underlies many of our unique strengths and vulnerabilities as a species - but efforts to understand its organization are challenged by reliance on incompatible measurement methods at different spatial scales. Macroscale features such as cortical folding or functional activation are accessed through spatially dense neuroimaging maps, whereas microscale cellular and molecular features are typically measured with sparse postmortem sampling. Here, we integrate these distinct windows on brain organization by building upon existing postmortem data to impute, validate and analyze a library of ~20,000 spatially dense neuroimaging-like maps of human cortical gene expression. These maps allow spatially unbiased discovery of cortical zones with extreme transcriptional profiles or unusually rapid transcriptional change indexing distinct microstructure. Comparison with neuroimaging shows these molecular transitions are aligned with cortical folding and functional specializations. Next, we define canonical cortex-wide gene co-expression patterns, and show that these integrate diverse spatial scales and temporal epochs of human brain organization - ranging from protein-protein interactions to large-scale systems for cognitive processing. These spatial modes of cortical gene expression are enriched for neuropsychiatric disorder risk genes, and - in the example of autism spectrum disorder - define a functionally enriched subset of risk genes that tags specific cyto-laminar features and predicts the location of altered cortical anatomy and gene expression in patients. Taken together, the methods, resources and findings described here advance our understanding of human cortical organization and offer flexible bridges to connect scientific fields operating at different spatial scales of human brain research.

Introduction

The human cerebral cortex is an astoundingly complex structure that underpins many of our distinctive facilities and vulnerabilities[1]. Achieving a mechanistic understanding of cortical organization in health and disease requires integrating information across its many spatial scales: from macroscale cortical folds and functional networks[2] to the gene expression programs that reflect microscale cellular and laminar features[3,4]. However, a hard obstacle to this goal is that our measures of the human cortex at macro- and microscales are fundamentally mismatched in their spatial sampling. Macroscale measures from in vivo neuroimaging provide spatially dense estimates of structure and function, but microscale measures of gene expression are gathered from spatial discontinuous postmortem samples that have so far only been linked to macroscale features using methodologically-imposed cortical parcellations[5–7]. Consequently, local transitions in human cortical gene expression remain uncharacterized and unintegrated with the spatially fine-grained topographies of human cortical structure and function that are revealed by in vivo neuroimaging[8,9]. Finding a way to bridge this gap would not only enrich both our micro- and macro-scale models of human cortical organization, but also provide an essential framework for translation across traditionally siloed scales of neuroscientific research.

Here, we use spatially sparse postmortem data from the Allen Human Brain Atlas [AHBA[3]] to generate and validate spatially dense cortical expression maps (DEMs) for 20,781 genes in the adult brain. These maps allow a fine-grained transcriptional cartography of the human cortex, which we integrate with diverse genomic, histological and neuroimaging resources to shed new light on several fundamental aspects of human cortical organization in health and disease. First, by focusing on local transitions in gene expression, we reveal a close spatial coordination between molecular and functional specializations of the cortex, and establish that the spatial orientation of cortical folding and functional activation is aligned with local tangential transitions in cortical gene expression. Next, by defining and deeply-annotating gene co-expression modules across the cortex we systematically link macroscale measures of cortical structure and function in vivo, to postmortem markers of laminar, cellular and temporal features of cortical microstructure from early fetal to late adult life. Finally, as a proof-of-principle, we use this novel framework to secure a newly-integrated multiscale understanding of atypical brain development in autism spectrum disorder (ASD).

The tools and results from this analysis of the human cortex - which we collectively call Multiscale Atlas of Gene expression for Integrative Cortical Cartography (MAGICC) - open up an empirical bridge that can now be used to connect cortical models (and scientists) that have so far operated at segregated spatial scales. To this end, we share: (i) all gene-level DEMs and derived transcriptional landscapes in neuroimaging-compatible files for easy integration with in vivo macroscale measures of human cortical structure and function; and (ii) all gene sets defining spatial subcomponents of cortical transcription for easy integration with any desired genomic annotation (MAGICC: share link).

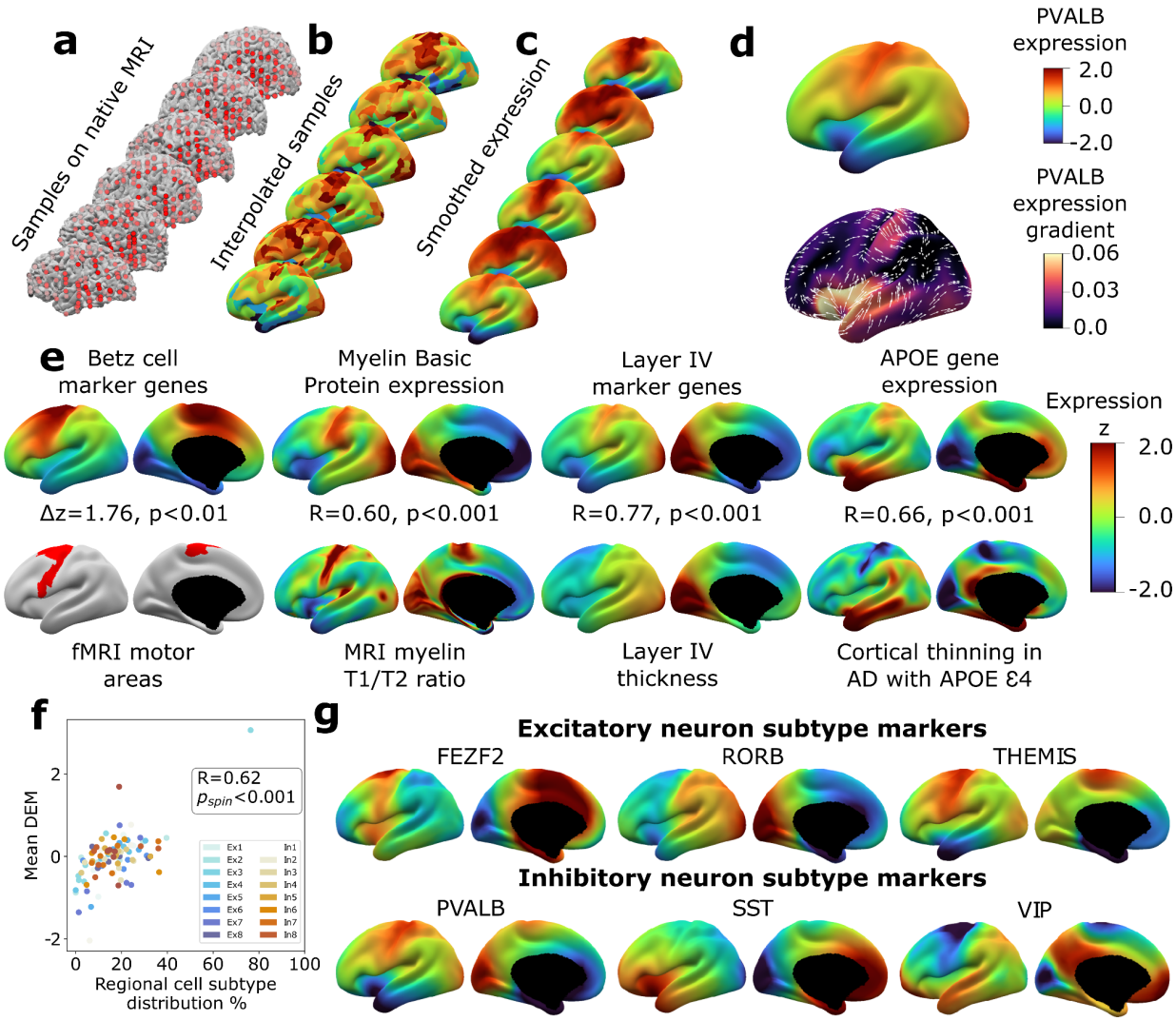

Figure 1. Creating and Benchmarking Spatial Dense Gene Expression Maps in the Human Cortex. ***a****, Spatially discontinuous Allen Human Brain Atlas (AHBA) microarray samples (red points) were aligned with MRI-derived cortical surface mesh reconstructions.* ***b****, AHBA vertex expression values were propagated using nearest-neighbor interpolation and subsequently smoothed* ***(c)****.* ***d,*** *Subject-level maps were z-normalized and averaged to generate a single reference dense expression map (DEM) for each gene, as well as the associated expression gradient map (shown here for PVALB: top and bottom, respectively).* ***e,*** *Illustrative comparisons of selected DEMs with corresponding macroscale cortical measures from independent neuroimaging and histological markers.* ***f****, Illustrative comparisons of selected DEMs against microscale cortical measures: scatterplot showing the global correlation of regional cellular proportions from single nucleus RNAseq (snRNAseq) across 16 cells and 6 regions[10] with DEM values for corresponding cell-type marker genes (R=0.48, p_{spin}<0.001, excluding Ex3-V1 and In8-BA10 outlier samples).* ***g****, DEMs for markers of 6 neuronal subtypes (3 excitatory: FEZF2, RORB, THEMIS, 3 inhibitory: PVALB, SST, VIP) based on recently validated subtype marker genes[11,12]*

Results

Creating and benchmarking spatially dense maps of human cortical gene expression

To create a dense transcriptomic atlas of the cortex, we used AHBA microarray measures of gene expression for 20,781 genes in each of 1304 cortical samples from six donor left cortical hemispheres (**Methods, Table S1**). We extracted a model of each donor's cortical sheet by processing their brain MRI scan, and identified the surface location (henceforth "vertex") of each postmortem cortical sample in this sheet (**Methods**, **Fig 1a**). For each gene, we then propagated measured expression values into neighboring vertices using nearest-neighbor interpolation followed by smoothing (**Methods**, **Fig 1b,c**). Expression values were scaled across vertices and these vertex-level expression maps were averaged across donors to yield a single dense expression map (DEM) for each gene - which provided estimates of expression at ~ 30,000 vertices across the cortical sheet (e.g. DEM for PVALB upper panel **Fig 1d**). These fine-grained vertex-level measures also enabled us to estimate the orientation and magnitude of expression change for each gene at every vertex (e.g. dense expression change map for PVALB, lower panel **Fig 1d**)

We assessed the reproducibility of DEMs by repeating the above process (**Fig 1**) after repeatedly splitting the donors into non-overlapping groups of varying size, and using learning curve analyses to estimate the DEM reproducibility achieved by our full set of 6 donors. For cortically expressed genes (**Methods, Table S2**), the average reproducibility of gene expression maps was r=0.56 (correlation of expression values for a gene across vertices), and the average reproducibility of ranked gene expression at each vertex was r=0.63 (correlation of expression values at a vertex across genes) (**Fig S1c-e**). These estimates were substantially lower for genes without recorded cortical expression (**Methods, Table S2**). Regional differences in the density of postmortem sampling in the AHBA did not influence DEM reproducibility or the magnitude of local expression change captured by DEMs (**Methods, Fig S1h**).

To assess the biological validity of DEMs across contrasting spatial scales, we drew on selected independent macro- and microscale cortical measures that DEMs should align with based on known biological processes (**Fig 1e,f,g, Methods**). At the macroscale, maps from diverse measurement modalities showed strong and statistically-significant spatial correlations with their corresponding DEM(s) relative to a null distribution based on random "spinning" of maps[13] (**Fig 1e, Methods,** all $p_{spin}<0.01$): (i) areas of cortex activated during motor fMRI tasks in humans[2] vs. the average DEM for canonical cell markers of large pyramidal neurons (Betz cells) found in layer V of the motor cortex that are the outflow for motor movements[11], (ii) an *in vivo* neuroimaging marker of cortical myelination (T1/T2 ratio[14]) vs. the Myelin Basic Protein DEM, which marks myelin (iii) the relative thickness of cortical layer IV[15] vs. the average DEM for layer IV marker genes[16–18], and (iv) the degree of in vivo regional cortical thinning by MRI in Alzheimer disease patients who have at least one APOE E4 variant[19,20] vs. the APOE DEM (thinning map generated from 119 APOE E4 patients and 633 controls structural MRI (sMRI) scans as detailed in **Methods**). For initial biological validation of DEMs at microscale, we harnessed regional differences in the proportion of canonical neuronal subtypes as described by single nucleus RNAseq (snRNAseq)[10]. We observed a strong spatial correlation (r=0.6, $p_{spin}<0.001$) between regional marker gene expression in DEMs and regional proportions of their corresponding

neuronal subtypes from snRNAseq (**Fig 1f, Methods**). **Fig 1g** shows example marker gene DEMs for 6 canonical neuronal subtypes: 3 excitatory (FEZF2, RORB, THEMIS) and 3 inhibitory (PVAL, SST, VIP)[11,12]. Collectively, the above tests of reproducibility (**Fig S1**) and convergent validity (**Fig 1e,f**) supported use of DEMs for downstream analyses.

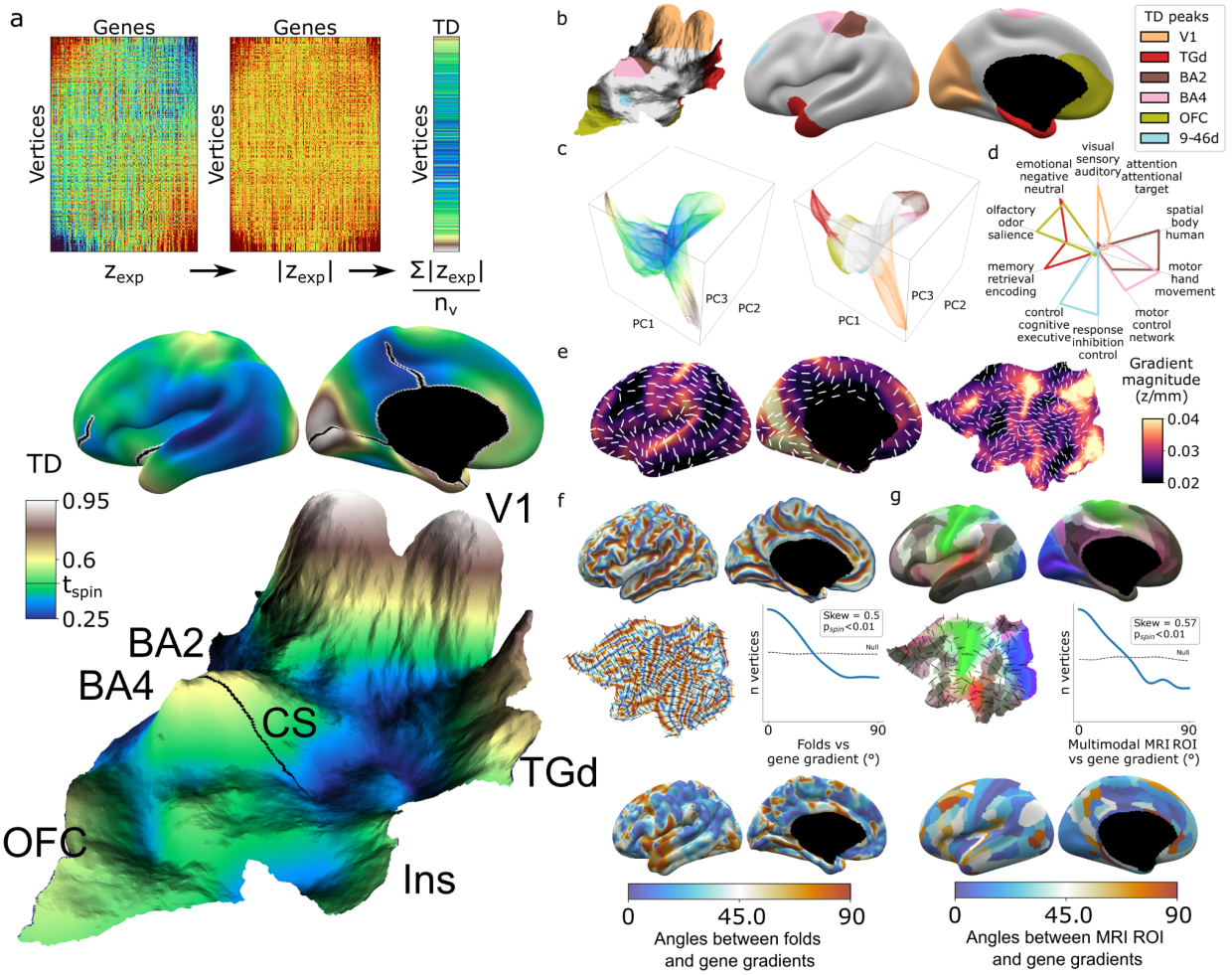

Figure 2. Mapping transcriptional distinctiveness in the human cortex and its alignment with macroscale structure and function. a, *Regional transcriptomic distinctiveness (TD) can be quantified as the mean absolute z-score of dense expression map (DEM) values at each vertex (top), and visualized as a continuous cortical map (middle, TD encoded by color) or in a relief map of the flattened cortical sheet (bottom, TD encoded by color and elevation,* ***Sup Movie 1****). Black lines on the inflated view identify cuts for the flattening procedure. The cortical relief map is annotated to show the central sulcus (CS), and peaks of TD overlying dorsal sensory and motor cortices (Brodmann Areas, BA2, BA4), the primary visual cortex (V1), temporal pole (TGd), insula (Ins) and ventromedial prefrontal cortex (OFC).* ***b,*** *Thresholding the TD map through spatial permutation of DEMs (t_{spin}* ***Methods****) and clustering significant vertices by their expression profile defined six TD peaks in the adult human cortex (depicted as coloured regions on terrain and inflated cortical surfaces).* ***c,*** *Cortical vertices projected into a 3D coordinate system defined by the first 3 principal components (PCs) of gene expression, coloured by the continuous TD metric (left) and TD peaks (right). TD peaks are focal anchors of cortex-wide expression PCs* ***d,*** *TD peaks show statistically-significant functional specializations in a meta-analysis of in vivo functional MRI data.* ***e,*** *The average magnitude of local expression transitions across genes (color) and principal orientation of these transitions (white bars) varies across the cortex.* ***f,*** *Cortical folds in AHBA donors (top surface maps and middle flat-map) tend to be aligned with the principal orientation of TD change across cortical vertices (p<0.01, middle histogram, sulci running perpendicular to TD change), and the strength of this alignment varies between cortical regions.* ***g****, Putative cortical areas defined by a multimodal in vivo MRI parcellation of the human cortex*[2] *(top surface maps and middle flat-map) also tend to be aligned with the principal direction of gene*

expression change across cortical vertices (p<0.01, middle histogram, sulci running perpendicular to long axis of area boundaries), and the strength of this alignment varies between cortical areas.

Defining and surveying the human cortex as a continuous transcriptional terrain

As an initial summary view of transcriptional patterning in the human cortex, we first averaged all 20,781 DEMs to represent the cortex as a single continuous transcriptional terrain, where altitude encodes the transcriptional distinctiveness (TD) of each cortical point (vertex) relative to all others (TD = mean(abs(z_{exp})), **Figure 2a**, **Sup Movie 1**). This terrain view revealed 6 statistically-significant TD peaks (**Methods**, **Fig. 2a,b**) which recover all major archetypal classes of the mammalian cortex as defined by classical studies of laminar and myelo-architecture, connectivity, and functional specialization[21] encompassing: primary visual (V1), somatosensory [Brodmann area (BA[22]) 2], and motor cortex (BA 4), as well limbic [temporal pole centered on dorsal temporal area G (TGd[23]), ventral frontal centered in orbitofrontal cortex (OFC)] and heteromodal association cortex (BA 9-46d). Of note, our agnostic parcellation of all TD peak vertices by their ranked gene lists (**Methods**) perfectly cleaved BA2 and BA4 along the central sulcus - despite there being no representation of this macroanatomical landmark in DEMs.

Integration with principal component analysis of DEMs across vertices (**Methods, Fig S2a,b**) showed that TD peaks constitute sharp poles of more recently-recognized cortical expression gradients[24] (**Fig. 2c**). The "area-like" nature of these TD peaks is reflected by the steep slopes of transcriptional change surrounding them (**Figure 2a,e**), and could be quantified as TD peaks being transcriptomically more distinctive than their physical distance from other cortical regions would predict (**Fig. S2c,d**). In contrast, transitions in gene expression are more gradual and lack such sharp transitions in the cortical regions between TD peaks (**Fig 2 a,c,e, Fig S2h**). Thus, because DEMs provide spatially fine-grained estimates of cortical expression and expression change, they offer an objective framework for arbitrating between area-based and gradient-based views of cortical organization in a regionally-specific manner.

The TD peaks defined above exist as discrete patches of cortex and the distinctive profile of gene expression which defines each peak, and this duality offers an initial bridge between macro- and microscale views of cortical organization. Specifically, we found that each TD peak overlapped with a functionally-specialized cortical region based on meta-analysis of in vivo functional neuroimaging data[25] (**Methods, Fig. 2d, Table S3**), and featured a gene expression signature that was preferentially enriched for a distinct set of biological processes, cell type signatures (**Fig S2e**) and cellular compartments (**Methods, Table S2 and S3**). For example, the peaks overlapping area TGd and OFC were enriched for synapse-related terms, while BA2 and BA4 TD peaks were predominantly enriched for metabolic and mitochondrial terms. At a cellular level, V1 closely overlapped with DEMs for marker genes of the Ex3 neuronal subtype known to be localised to V1(Lake et al. 2016), while BA4 closely overlapped Betz cell markers(Bakken et al. 2021) (**Fig S2e**).

The expression profile of each TD peak was achieved through surrounding zones of rapid transcriptional change (**Fig 2a,e, Fig S2f,g**). We noted that these transition zones tended to overlap with cortical folds - suggesting an alignment between spatial orientations of gene expression and folding. To formally test this idea we defined the dominant orientation of gene expression change at each vertex (**Methods, Fig 2e**) and computed the angle between this and

the orientation of folding (**Methods**). The observed distribution of these angles across vertices was significantly skewed relative to a null based on random alignment between angles (p_{spin}<0.01, **Fig 2f, Methods**) - indicating that there is indeed a tendency for cortical sulci to run perpendicular to the direction of fastest transcriptional change (p_{spin}<0.01, **Fig 2f**). A similar alignment was seen when comparing gradients of transcriptional change with the spatial orientation of putative cortical areas defined by multimodal in vivo neuroimaging[2] (expression change running perpendicular to area long-axis, p_{spin}<0.01, **Fig 2g, Methods**). Visualizing these expression-folding and expression-areal alignments revealed greatest concordance over sensorimotor, medial occipital, cingulate, and posterior perisylvian cortices (with notable exceptions of transcription change running parallel to sulci and the long-axis of putative cortical areas in lateral temporoparietal and temporopolar regions). As a preliminary probe for causality, we examined the developmental ordering of regional folding and regional transcriptional identity. Mapping the expression of high-ranking TD genes in fetal cortical laser dissection microarray data[26] from 21 PCW (Post Conception Weeks) (**Methods**) showed that the localized transcriptional identity of V1 and TGd regions in adulthood is already apparent well before these cortical regions show mature folding topology[27] (**Fig S2h**). Thus, the unique capacity of DEMs to resolve local orientations of expression change reveals a close spatial alignment between regional transitions of cortical gene expression at microscale and regional transitions of cortical folding, structure and function at macroscale.

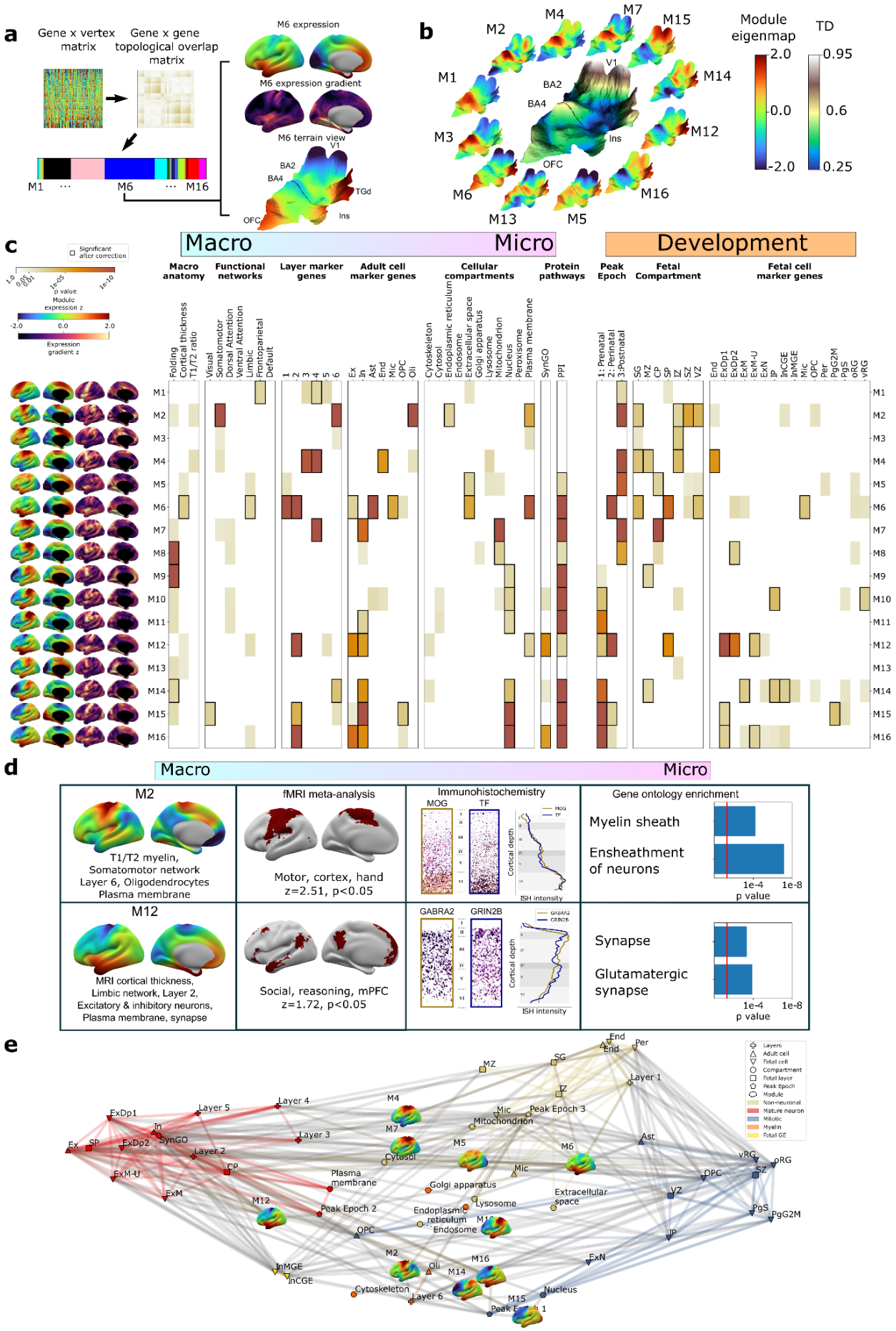

Figure 3. Cortex-wide Gene Coexpression Patterns Reflect Multiple Spatial Scales and Developmental Epochs of Brain Organization. a, *Overview of Weighted Gene Co-expression Network Analysis (WGCNA) pipeline applied to the full DEM dataset. Starting top left: the pairwise DEM spatial correlation matrix is used to generate a topological overlap matrix between genes (middle top) which is then clustered. Of the 23 WGCNA-defined modules, 7 were significantly enriched for non-cortical genes and removed, leaving 16 modules. Each module is defined by a set of spatially co-expressed genes, for which the principal component of expression can be computed and mapped at each cortical point. M6 is shown as an example projected onto an inflated left hemisphere (M6 z-scored expression and M6 expression change), and the bulk transcriptional distinctiveness (TD) terrain view from* ***Fig 2*** *(M6 expression).* ***b,*** *The extremes of module eigenmaps highlight different peaks in the cortical terrain: the main TD terrain colored by TD value (center, from* ***Fig 2****), surrounded by TD terrain projections of selected WGCNA Module expression eigenmaps.* ***c,*** *WGCNA modules (eigenmaps and gradient maps, rows) are enriched for multiscale aspects of cortical organization (columns). Cell color intensity indicates pairwise statistical significance ($p<0.05$), while black outlines show significance after correction for multiple comparisons across modules. Columns capture key levels of cortical organization at different spatial scales (arranged from macro- to microscale) and developmental epochs: spatial alignment between module eigenmaps and in vivo MRI maps of cortical folding orientation, cortical thickness and T1/T2 ratio, fMRI resting-state functional networks; enrichment for module gene sets for independent annotations (****Table S2****) marking: cortical layers*[17,18]*; cell types*[10,12,28–34]*; subcellular compartments*[35]*; synapse-related genes*[36]*; protein-protein interactions between gene products* [37]*; temporal epochs of peak expression*[38] *["fetal": 8-24 21 post conception weeks (PCW) / "perinatal'' 24 PCW-6 months / "postnatal" >6 months]; transient layers of the mid-fetal human cortex at 21 post conception weeks (PCW)*[26] *[subpial granular zone (SG), marginal zone (MZ), cortical plate (CP), subplate (SP), intermediate zone (IZ), subventricular zone (SZ) and ventricular zone (VZ)]; and fetal cell types at 17-18 PCW*[39]*.* ***d,*** *Independent validation of multiscale enrichments for selected modules M2 & M12. M2 significantly overlaps the Neurosynth topic associated with the terms motor, cortex and hand. Two high-ranking M2 genes, MOG & TF exhibit clear layer VI peaks on ISH and GO enrichment analysis myelin-related annotations. M12, overlapping the limbic network most closely overlapped the Neurosynth topic associated with social reasoning. Two high-ranking M22 genes GABRA2 and GRIN2B showed layer II ISH peaks and GO enrichment analysis revealed synaptic annotations.* ***e****, Network visualization of pairwise overlaps between annotational gene sets used in* ***Fig 3c****, including WGCNA module gene sets (inset expression eigenmaps).*

Cortical gene coexpression integrates diverse spatial scales of human brain organization

To complement the TD analyses above (**Fig 2**), we next used weighted gene co-expression network analysis (WGCNA[40], **Methods**, **Fig 3a**) to achieve a more systematic integration of macro- and macroscale cortical features. This integration is enabled by the fact that each WGCNA module exists as both (i) a single expression map (eigenmap) for spatial comparison with neuroimaging data (**Fig 3a,b**, **Methods**) and, (ii) a unique gene set for enrichment analysis against marker genes for cortical layers, cell types, cell compartments, protein-protein interactions (PPI) and GO terms (**Methods**, **Table S2 and S4**). Furthermore, whereas prior applications of WGCNA to AHBA data have revealed gene sets that covary in expression across many different compartments of the brain[4,41,42], using DEMs as input to WGCNA generates modules that are purely based on the fine-scale coordination of gene expression across the cortex. Using WGCNA, we identified 16 gene modules (M1-M16), which we then deeply annotated against independent measures of cortical organization at diverse spatial scales and developmental epochs (**Figure 3c, Methods**).

Several WGCNA modules showed statistically significant alignments with structural and functional features of the adult cerebral cortex from in vivo imaging (**Methods**, **Fig 3c**[14,43]). For

example, (i) the M6 eigenmap was significantly positively correlated with in vivo measures of cortical thickness from sMRI and enriched within a limbic functional connectivity network defined by resting state functional connectivity MRI, and (ii) the M8, M9 and M14 eigenmaps showed gradients of expression change that were significantly aligned with the orientation of cortical folding (especially around the central sulcus, medial prefrontal and temporo-parietal cortices, **Fig S3a**). At microscale, several WGCNA module gene sets showed statistically significant enrichments for genes marking specific cortical layers[17,18] and cell types[10,12,28–34] (**Methods**, **Fig 3c, Table S4**). These microscale enrichments were often congruent between cortical layers and cell classes annotations, and in keeping with the linked eigenmap (**Fig 3c**, **Table S4**). For example, M4 - which was uniquely co-enriched for markers of endothelial cells and middle cortical layers - showed peak expression over dorsal motor cortices which are known to show expanded middle layers[11,15] with rich vascularization[44] relative to other cortical regions. Similarly, M6 - which was enriched for markers of astrocytes, microglia and excitatory neurons as well as layers 1/2 - showed peak expression over rostral frontal and temporal cortices which are known to possess relatively expanded supragranular layers[15] that predominantly contain the apical dendrites of excitatory neurons and supporting glial cells[23]. We also observed that modules with similar eigenmaps (**Fig S3b**) (including overlaps of multiple modules with the same TD peak) could show contrasting gene set enrichments. For example M2 and M4 both showed peak expression of dorsal sensorimotor cortex (i.e. TD areas BA2 and BA4), but M2 captures a distinct architectonic signature of sensorimotor cortex from the mid-layer vascular signal of M4: expanded and heavily myelinated layer 6 [11,15,45] (**Fig 3c**). The spatially co-expressed gene modules detected by WGCNA were not only congruently co-enriched for cortical layer and cell markers, but also for nanoscale features such as sub-cellular compartments[35] (**Table S2 and S4**) (often aligning with the cellular enrichments) and protein-protein interactions[37] (PPI) (**Methods**, **Fig 3c, Table S4**). This demonstrates the capacity of our resource to tease apart subtle subcomponents of neurobiology based on cortex-wide expression patterns.

To further assess the robustness of these multiscale relationships, we focused on two modules with contrasting multiscale signatures - M2 and M12 - and tested for reproducibility of our primary findings (**Fig 3c**) using orthogonal methods. Our primary analyses indicated that M2 has an expression eigenmap which overlaps with the canonical somato-motor network from resting-state functional neuroimaging[43], and contains genes that are preferentially expressed in cortical layer 6 from layer-resolved transcriptomics[17,18], and in oligodendrocytes from snRNAseq[10,12,28–34] (**Fig 3c**). We were able to verify each of these observations through independent validations including: spatial overlap of M2 expression with meta analytic functional activations relating to motor tasks[25]; immunohistochemistry localization of high-ranking M2 genes to deep cortical layers[16] (**Methods**); and significant enrichment of M2 genes for myelin-related GO terms (**Fig 3d, Table S4**). By contrast, our primary analyses indicated that M12 - which had peak expression over ventral frontal and temporal limbic cortices - was enriched for marker genes for layer 2, neurons and the synapse (**Fig 3c**). These multiscale enrichments were all supported by independent validation analyses, which showed that: the M12 eigenmaps is enriched in a limbic network that is activated during social reasoning[25]; high-ranking M12 marker genes show elevated expression in upper cortical layers by immunohistochemistry[16] (**Methods**);

and, there is a statistically-significant over representation of synapse compartment GO terms in the M12 gene set (**Fig 3d, Table S4**).

Linking spatial and developmental aspects of cortical organization

Given that adult cortical organization is a product of development, we next asked if eigenmaps of adult cortical gene expression (**Fig 3a,b**) are related to the patterning of gene expression between fetal stages and adulthood. To achieve this, we tested WGCNA module gene sets for enrichment of developmental marker genes from 3 independent postmortem studies (rightmost columns, **Fig 3c**) capturing genes with differential expression between (i) 3 developmental epochs between 8 post-conception weeks (PCWs) and adulthood (*BrainVar* dataset from prefrontal cortex[38]) (ii) 7 histologically-defined zones of mid-fetal (21 PCW) cortex[26] (**Methods**, **Table S1 and S2), and (iii)** 16 mid-fetal (17-18 PCW) cell-types[39] (**Methods, Table S2**).

Comparison with the *BrainVar* dataset revealed that most module eigenmaps (13 of all 16 cortical modules) were enriched for genes with developmentally-dynamic expression levels between early fetal and late adult stages (**Figure 3c, Table S4**). This finding was reinforced by supplementary analyses modeling developmental trajectories of eigenmap gene set expression between 12 PCW and 40 years in the *BrainSpan* dataset[33] (**Methods**, **Fig S3c**), and further qualified by the observation that several WGCNA modules were also differentially enriched for markers of mid-fetal cortical layers and cell-types[26,39] (**Figure 3c, Table S4**). As observed for multiscale spatial enrichments (**Fig 3c,d**); the developmental enrichments of modules were often closely coordinated with one another, and eigenmaps with similar patterns of regional expression could possess different signatures of developmental enrichment. For example, the M6 and M12 eigenmaps shared a similar spatial expression pattern in the adult cortex (peak expression in medial prefrontal, anterior insula and medio-ventral temporal pole), but captured different aspects of human brain development that aligned with the cyto-laminar enrichments of M6 and M12 in adulthood. The M6 gene set - which was enriched for predominantly glial elements of layers 1 and 2 in adult cortex - was also enriched for markers of mid-fetal microglia[39], the transient fetal layers that are known to be particularly rich in mid-fetal microglia (subpial granular, subplate , and ventricular zone[46]), and the mid-late fetal epoch when most microglial colonization of the cortex is thought to be achieved[47] (**Fig 3c**). In contrast, the M12 gene set - which was enriched for predominantly neuronal elements of layer 2 in adult cortex - also showed enrichment for marker genes of developing fetal excitatory neurons, the fetal cortical subplate, and windows of mid-late fetal development when developing neurons are known to be migrating into a maximally expanded subplate[48].

The striking co-enrichment of WGCNA modules for features of both the fetal and adult cortex (**Fig 3c**) implied a patterned sharing of marker genes between cyto-laminar features of the adult and fetal cortex, despite the fact that many fetal cell types and cortical compartments are no longer apparent in adulthood. To more directly test this idea, and characterize potential biological themes reflected by these shared marker genes, we carried out pairwise enrichment analyses between all annotational gene sets from **Fig 3c**. These gene sets collectively draw from a diverse array of study designs encompassing bulk, laminar, and single cell transcriptomics of the human cortex between 10 PCW and 60 years of life (**Methods**[17,18,26,29–34,38,39]). Network visualization and clustering of the resulting adjacency matrix (**Fig S3d**) revealed an integrated

annotational space defined by five coherent clusters (**Fig 3e**). A mature neuron cluster encompassed markers of post-mitotic neurons and the compartments that house them in both fetal and adult cortex (red, **Fig 3e, Table S2**, example core genes: NRXN1, SYT1, CACNG8). This cluster also included genes with peak expression between late fetal and early postnatal life, and those localizing to the plasma membrane and synapse. A small neighboring fetal ganglionic eminence cluster (Fetal GE, yellow, **Fig 3e, Table S2**, example core genes: NPAS3, DSX, DCLK2) contained marker sets for migrating inhibitory neurons from the medial and caudal ganglionic eminence in mid-fetal life. These two neuronal clusters - mature neuron and Fetal GE - were most strongly connected to the M12 gene set (**Methods**), which highlights medial prefrontal, and temporal cortices possessing a high ratio of neuropil:neuronal cell bodies[49,50]. A mitotic annotational cluster (blue, **Fig 3e, Table S2**, example core genes: CCND2, MEIS2, PHLDA1) was most distant from these two neuronal clusters, and included genes showing highest expression in early development as well as markers of cycling progenitor cells, radial glia, oligodendrocyte precursors, germinal zones of the fetal cortex, and the nucleus. This cluster was most strongly connected to the M15 gene set, which shows high expression over occipito-parietal cortices distinguished by a high cellular density and notably low expression in lateral prefrontal cortices, which possess low cellular density[51]. The mature neuron and mitotic clusters were separated by two remaining annotational clusters for non-neuronal cell types and associated cortical layers. A myelin cluster (orange, **Fig 3e, Table S2**, example core genes: MOBP, CNP, ACER3) - which contained gene sets marking adult layer 6, oligodendrocytes, and organelles supporting the distinctive biochemistry and morphology of oligodendrocytes (the golgi apparatus, endoplasmic reticulum and cytoskeleton) - was most connected to the M2 gene set highlighting heavily myelinated motor cortex[52]. A non-neuronal cluster (yellow, **Fig 3e, Table S2**, example core genes: TGFBR2, GMFG, A2M) - which encompassed marker sets for microglia, astrocytes, endothelial cells, pericytes, and markers of superficial adult and fetal cortical layers that are relatively depleted of neurons - was most connected to the M6 gene set highlighting medial temporal and anterior cingulate cortices with notably high non-neuronal content[49].

These analyses show that the regional patterning of bulk gene expression captures the organization of the human cortex across multiple spatial scales and developmental stages such that (i) the summary expression maps of spatially co-expressed gene sets align with independent in vivo maps of macroscale structure and function from neuroimaging, while (ii) the spatially co-expressed gene sets defining these maps show congruent enrichments for specific adult cortical layers and cell-types as well as developmental precursors of these features spanning back to mid-fetal life.

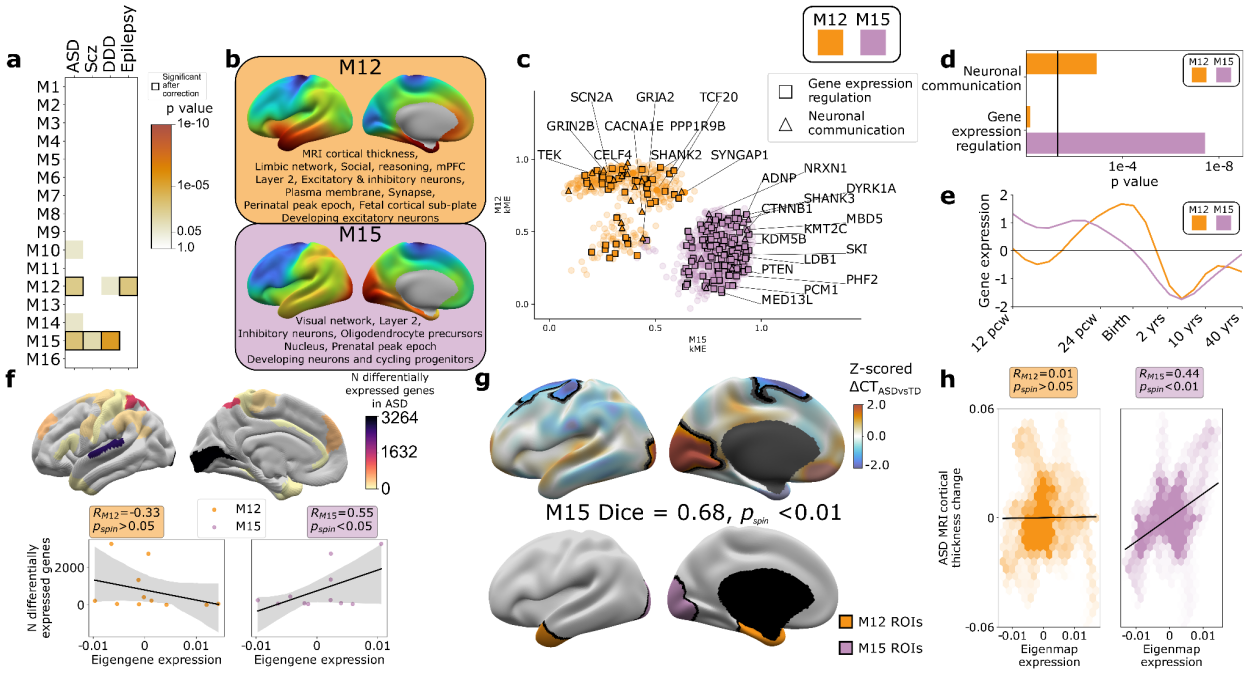

Figure 4. ***ASD risk genes follow two different spatial patterns of cortical gene expression which differentially predict cortical changes in ASD. a,*** *Enrichment of WGCNA module gene sets for risk genes associated with atypical brain development through enrichment of rare deleterious variants in studies of Autism Spectrum Disorder (ASD), Schizophrenia (Scz), severe developmental disorders (DDD, Deciphering Developmental Disorders study) and Epilepsy. Cell color intensity indicates pairwise statistical significance (p<0.05), while outlined matrix cells survived correction for multiple comparisons across modules.* ***b****, Summary of multiscale and developmental annotations from* ***Fig 3c*** *for M12 and M15: the only two WGCNA modules enriched for risk genes of more than one neurodevelopmental disorder.* ***c****, M12 and M15 genes clustered by the strength of their membership to each module. Color encodes module membership. Shape encodes annotations for two GO Biological Process annotations that differ between the module gene sets: neuronal communication and regulation of gene expression. Text denotes specific ASD risk genes.* ***d****, contrasting GO enrichment of M12 and M15 for neuronal communication and regulation of gene expression GO Biological Process annotations.* ***e****, M12 and M15 differ in the developmental trajectory of their average cortical expression between early fetal and mid-adult life*[33]*.* ***f****, Regional differences in intrinsic expression of the M15 module (but not the M12 module) in adult cortex is correlated with regional variation in the severity of altered cortical gene expression (number of differentially expressed genes) in ASD*[53]*.* ***g****, Statistically-significant regional alterations of cortical thickness (CT) in ASD compared to typically developing controls from in vivo neuroimaging*[54,55] *(top). Areas of cortical thickening show a statistically-significant spatial overlap (Dice overlap = 0.68,* p_{spin}*<0.01) with regions of peak intrinsic expression for M15 in adult cortex (bottom).* ***h****, M15 eigenmap expression (but not M12 eigenmap) shows significant spatial correlation with relative cortical thickness change in ASD.*

ASD risk genes follow two different spatial patterns of cortical expression, which capture distinct aspects of cortical organization and differentially predict cortical changes in ASD

The findings above establish that gene co-expression modules in the human cortex capture multiple levels of biological organization ranging from subcellular organelles, to cell types, cortical layers and macroscale patterns of brain structure and function. Given that genetic risks for atypical brain development presumably play out through such levels of biological organization, we hypothesized that disease associated risk genes would be enriched within

WGCNA module gene sets. Testing this hypothesis simultaneously offers a means of further validating our analytic framework, while also potentially advancing understanding of disease biology. To test for disease gene enrichment in WGCNA modules, we compiled lists of genes enriched for deleterious rare variants in autism spectrum disorder[56,57] (ASD), schizophrenia[58] (SCZ), severe developmental disorders[59] and epilepsy[60] (**Table S2**). We considered rare (as opposed to common) genetic variants to focus on high effect-size genetic associations and avoid ongoing uncertainties regarding the mapping of common variants to genes[61]. We observed that disease associated gene sets were significantly enriched in several WGCNA modules (**Fig 4a**), with two modules showing enrichments for more than one disease: M15 (ASD, SCZ and DDD) and M12 (ASD and Epilepsy). ASD was the only disorder to show a statistically-significant enrichment of risk genes within both M12 and M15 (**Fig 4a**) - providing an ideal setting to ask if and how this partitioning of ASD risk genes maps onto (i) multiscale brain organization in health, and (ii) altered brain organization in ASD.

The eigenmaps and gene set enrichments of M12 vs. M15 implicated two contrasting multiscale motifs in the biology of ASD (**Fig 4b**). ASD risk genes including SCN2A, SYNGAP1, and SHANK2 resided within the M12 module (**Fig 4c**) which is most highly expressed within a distributed cortical system that is activated during social reasoning tasks (p_{spin}<0.01, **Fig 3c,d**, **Fig 5b**). The M12 gene set is also enriched for: genes with peak cortical expression in late-fetal and early postnatal life; marker genes for the fetal subplate and developing excitatory neurons; markers of layer 2 and mature neurons in adult cortex; and synaptic genes involved in neuronal communication (**Fig 3c,d**, **Fig 4b,c,d,e**, **Table S4**). In contrast, ASD risk genes including ADNP, KMT5B, and MED13L resided within the M15 module (**Fig 5c**), which is most highly expressed in primary visual cortex and associated ventral temporal pathways for object recognition/interpretation[62] (p_{spin}<0.05, **Fig 3c,d**, **Fig 4b, Table S4**). The M15 module is also enriched for: genes showing peak cortical expression in early fetal development, marker genes for cycling progenitor cells in the fetal cortex; markers of layer 2, inhibitory neurons and oligodendrocyte precursors in the adult cortex (**Fig 3c,d**, **Fig 4b,c,d,e, Table S4**). The alignment of ASD risk genes with M12 and M15 was reinforced when considering all 135 ASD risk genes: spatial co-expression analyses split these genes into two clear subsets with mean expression maps that most closely resembled M12 & M15 (**Fig S4a,b**). Thus - using only spatial patterns of cortical gene expression in adulthood, our analytic framework was able to recover the previous PPI and GO-based partitioning of ASD risk genes into synaptic vs. nuclear chromatin remodeling pathways[57,63], and then place these pathways into a richer biological context based on the known multiscale associations of M12 and M15 (**Figs 3c, 4a**).

We next sought to address whether regional differences in M12 and M15 expression were related to regional cortical changes observed in ASD. To test this idea, we used two orthogonal indices of cortical change in ASD that capture different levels of biological analysis - the number of differentially expressed genes (DEGs) postmortem[53], and the magnitude of changes in cortical thickness (CT) as measured by in vivo sMRI[55]. Regional DEG counts were derived from a recent postmortem study of 725 cortical samples from 11 cortical regions in 112 ASD cases and controls[53], and compared with mean M12 and M15 expression within matching areas of a multimodal MRI cortical parcellation[2]. The magnitude of regional transcriptomic disruption in ASD was statistically-significantly positively correlated with region expression of the M15 module

(r=0.6, p_{spin}<0.05), but not the M12 module (r=-0.3, p_{spin}>0.05) (**Fig 4f**). This dissociation is notable because M15 (but not M12) is enriched for genes involved in the regulation of gene expression (**Fig 4d**). Thus the enrichment of ASD risk genes within M15, and the intrinsically high expression of M15 in occipital cortex may explain why the occipital cortex is a hotspot of altered gene expression in ASD.

To compare M12 and M15 expression with regional variation in cortical anatomy changes in ASD, we harnessed the multicenter ABIDE datasets containing brain sMRI scans from 751 participants with idiopathic ASD and 773 controls[54,55]. We preprocessed all scans using well-validated tools for harminonized[64] estimation [64] of cortical thickness (CT)[64] from multicenter data (**Methods**), and then modeled CT differences between ASD and control cohorts at 150,000 points (vertices) across the cortex (**Methods**). This procedure revealed two clusters of statistically-significant CT change in ASD (**Methods**, **Fig 4g**, upper panel) encompassing visual and parietal cortices (relative cortical thickening vs. controls) as well as superior frontal vertices (relative cortical thinning). The occipital cluster of cortical thickening in ASD showed a statistically-significant spatial overlap with the cluster of peak M15 expression (**Fig 4g**, upper panel, **Methods**, Dice coefficient = 0.7, p_{spin}<0.01), and relative cortical thickness change correlated with the M15 eigenmap (**Fig 4h**). In contrast, M12 expression was not significantly aligned with CT change in ASD (**Fig 4g,h**). Testing these relationships in the opposite direction - i.e. asking if regions of peak M12 and M15 expression are enriched for directional CT change in ASD relative to other cortical regions - recovered the M15-specific association with regional cortical thickening in ASD (**Fig S4c**).

Taken together, the above findings reveal that an occipital hotspot of altered gene expression and cortical thickening in ASD overlaps with an occipital hotspot of high expression for a subset of ASD risk genes. These ASD risk genes are spatially co-expressed in a module enriched for several connected layers of biological organization (**Fig 3c, 4b,c,d**) spanning: nuclear pathways for chromatin modeling and regulation of gene expression; G2/M phase cycling progenitors and excitatory neurons in the mid-fetal cortex; oligodendrocytes and layer 2 cortical neurons in adult cortex; and occipital functional networks involved in visual processing. These multiscale aspects of cortical organization can now be prioritized as potential targets for a subset of genetic risk factors in ASD, and the logic of this analysis in ASD can now be generalized to any disease genes of interest.

Discussion

We build on the most anatomically comprehensive dataset of human cortex gene expression available to date[3], to generate, validate, characterize, apply and share spatially dense measures of gene expression that capture the topographically continuous nature of the cortical mantle. By representing patterns of human cortical gene expression without the imposition of a priori boundaries[24,41] our library of dense gene expression maps (DEMs) allows anatomically-unbiased analyses of local gene expression levels as well as the magnitudes and directions of local gene expression change. This core spatial property of DEMs unlocks several methodological and biological advances. First, the unparcellated nature of DEMs allows us to agnostically define cortical zones with extreme transcriptional profiles or unusually rapid transcriptional change - which we show to capture microstructural cortical properties and align with folding and functional specializations at the macroscale (**Fig 2**). By establishing that some of these cortical

zones are evident before cortical folding, we lend support to a "protomap"[65] like model where the placement of some cortical folds is set-up by rapid tangential changes in cyto-laminar composition of the developing cortex[66–68]. Second, we use spatial correlations between DEMs to decompose the complex topography of cortical gene expression into a smaller set of cortex-wide transcriptional programs that capture distinct aspects of cortical biology - at multiple spatial scales and multiple developmental epochs (**Fig 3**). This effort provides an integrative model that links expression signatures of cell-types and layers in prenatal life to the large-scale patterning of regional gene expression in the adult cortex, which can in turn - through DEMs - be compared to the full panoply of in vivo brain phenotypes provided by modern neuroimaging. Third, we find that some of these cortex-wide expression programs in adulthood are enriched for disease risk genes, and we show that the expression topography for a functionally-enriched subset of ASD risk genes can predict regional changes of gene expression and cortical thickness in ASD (**Fig 4**). The multiscale annotations of this spatially co-expressed set of risk genes propose specific cortical layers, cell-types, subcellular compartments, biological processes and developmental stages that may translate genetic risk into altered cortical organization in ASD. Crucially, the strategy applied in our analysis of ASD risk genes can be generalized to risk genes for any brain disorder of interest to place known risk factors for disease into the rich context of multiscale cortical biology.

Finally, the collection of DEMs, annotational gene sets and statistical tools used in this work (NAME) is shared as a new resource to accelerate multiscale neuroscience by allowing flexible and spatially unbiased translation between genomic and neuroanatomical spaces. Of note, this resource can easily incorporate any future expansions of brain data in either neuroanatomical or genomic space. We anticipate that it will be particularly valuable to incorporate new data from the nascent, but rapidly expanding fields of high throughput histology[15], single cell-omics[11], and large-scale imaging-genetics studies[69]. Taken together, MAGICC enables a new integrative capacity in the way we study the brain, and hopefully serves to spark new connections between previously distant datasets, ideas and researchers.

References

1. Geschwind, D. H. & Rakic, P. Cortical evolution: judge the brain by its cover. *Neuron* **80**, 633–647 (2013).
2. Glasser, M. F. *et al.* A multi-modal parcellation of human cerebral cortex. *Nature* **536**, 171–178 (2016).
3. Hawrylycz, M. J. *et al.* An anatomically comprehensive atlas of the adult human brain transcriptome. *Nature* **489**, 391–399 (2012).
4. Kelley, K. W., Nakao-Inoue, H., Molofsky, A. V. & Oldham, M. C. Variation among intact tissue samples reveals the core transcriptional features of human CNS cell classes. *Nat. Neurosci.* **21**, 1171–1184 (2018).
5. Seidlitz, J. *et al.* Transcriptomic and cellular decoding of regional brain vulnerability to neurogenetic disorders. *Nat. Commun.* **11**, 3358 (2020).
6. Larivière, S. *et al.* The ENIGMA Toolbox: multiscale neural contextualization of multisite neuroimaging datasets. *Nature Methods* vol. 18 698–700 (2021).
7. Hansen, J. Y. *et al.* Mapping gene transcription and neurocognition across human neocortex. *Nature Human Behaviour* vol. 5 1240–1250 (2021).
8. Gryglewski, G. *et al.* Spatial analysis and high resolution mapping of the human whole-brain transcriptome for integrative analysis in neuroimaging. *Neuroimage* **176**, 259–267 (2018).
9. Markello, R. D. *et al.* Standardizing workflows in imaging transcriptomics with the abagen toolbox. *Elife* **10**, (2021).
10. Lake, B. B. *et al.* Neuronal subtypes and diversity revealed by single-nucleus RNA sequencing of the human brain. *Science* **352**, 1586–1590 (2016).
11. Bakken, T. E. *et al.* Comparative cellular analysis of motor cortex in human, marmoset and

mouse. *Nature* **598**, 111–119 (2021).

12. Hodge, R. D. *et al.* Conserved cell types with divergent features in human versus mouse cortex. *Nature* **573**, 61–68 (2019).
13. Alexander-Bloch, A. F. *et al.* On testing for spatial correspondence between maps of human brain structure and function. *Neuroimage* **178**, 540–551 (2018).
14. Glasser, M. F. & Van Essen, D. C. Mapping human cortical areas in vivo based on myelin content as revealed by T1- and T2-weighted MRI. *J. Neurosci.* **31**, 11597–11616 (2011).
15. Wagstyl, K. *et al.* BigBrain 3D atlas of cortical layers: Cortical and laminar thickness gradients diverge in sensory and motor cortices. *PLoS Biol.* **18**, e3000678 (2020).
16. Zeng, H. *et al.* Large-scale cellular-resolution gene profiling in human neocortex reveals species-specific molecular signatures. *Cell* **149**, 483–496 (2012).
17. He, Z. *et al.* Comprehensive transcriptome analysis of neocortical layers in humans, chimpanzees and macaques. *Nat. Neurosci.* **20**, 886–895 (2017).
18. Maynard, K. R. *et al.* Transcriptome-scale spatial gene expression in the human dorsolateral prefrontal cortex. *Nat. Neurosci.* **24**, 425–436 (2021).
19. Gutiérrez-Galve, L. *et al.* Patterns of cortical thickness according to APOE genotype in Alzheimer's disease. *Dement. Geriatr. Cogn. Disord.* **28**, 476–485 (2009).
20. LaMontagne, P. J. *et al.* OASIS-3: Longitudinal neuroimaging, clinical, and cognitive dataset for normal aging and Alzheimer disease. *bioRxiv* (2019) doi:10.1101/2019.12.13.19014902.
21. Mesulam, M. M. From sensation to cognition. *Brain* **121 (Pt 6)**, 1013–1052 (1998).
22. Brodmann, K. *Vergleichende Lokalisationslehre der Grosshirnrinde in ihren Prinzipien dargestellt auf Grund des Zellenbaues*. (Barth, 1909).
23. von Economo, C. F. & Koskinas, G. N. *Die cytoarchitektonik der hirnrinde des erwachsenen menschen*. (J. Springer, 1925).

24. Burt, J. B. *et al.* Hierarchy of transcriptomic specialization across human cortex captured by structural neuroimaging topography. *Nat. Neurosci.* **21**, 1251–1259 (2018).
25. Yarkoni, T., Poldrack, R. A., Nichols, T. E., Van Essen, D. C. & Wager, T. D. Large-scale automated synthesis of human functional neuroimaging data. *Nat. Methods* **8**, 665–670 (2011).
26. Miller, J. A. *et al.* Transcriptional landscape of the prenatal human brain. *Nature* **508**, 199–206 (2014).
27. Chi, J. G., Dooling, E. C. & Gilles, F. H. Gyral development of the human brain. *Ann. Neurol.* **1**, 86–93 (1977).
28. Lake, B. B. *et al.* Integrative single-cell analysis of transcriptional and epigenetic states in the human adult brain. *Nat. Biotechnol.* **36**, 70–80 (2018).
29. Ruzicka, B. *et al.* Single-Cell Dissection of Schizophrenia Reveals Neurodevelopmental-Synaptic Link and Transcriptional Resilience Associated Cellular State. *Biol. Psychiatry* **89**, S106 (2021).
30. Velmeshev, D. *et al.* Single-cell genomics identifies cell type-specific molecular changes in autism. *Science* **364**, 685–689 (2019).
31. Habib, N. *et al.* Massively parallel single-nucleus RNA-seq with DroNc-seq. *Nat. Methods* **14**, 955–958 (2017).
32. Darmanis, S. *et al.* A survey of human brain transcriptome diversity at the single cell level. *Proc. Natl. Acad. Sci. U. S. A.* **112**, 7285–7290 (2015).
33. Li, M. *et al.* Integrative functional genomic analysis of human brain development and neuropsychiatric risks. *Science* **362**, (2018).
34. Zhang, Y. *et al.* Purification and Characterization of Progenitor and Mature Human Astrocytes Reveals Transcriptional and Functional Differences with Mouse. *Neuron* **89**, 37–53 (2016).

35. Binder, J. X. *et al.* COMPARTMENTS: unification and visualization of protein subcellular localization evidence. *Database* **2014**, bau012 (2014).

36. Koopmans, F. *et al.* SynGO: An Evidence-Based, Expert-Curated Knowledge Base for the Synapse. *Neuron* **103**, 217–234.e4 (2019).

37. Szklarczyk, D. *et al.* STRING v11: protein-protein association networks with increased coverage, supporting functional discovery in genome-wide experimental datasets. *Nucleic Acids Res.* **47**, D607–D613 (2019).

38. Werling, D. M. *et al.* Whole-Genome and RNA Sequencing Reveal Variation and Transcriptomic Coordination in the Developing Human Prefrontal Cortex. *Cell Rep.* **31**, 107489 (2020).

39. Polioudakis, D. *et al.* A Single-Cell Transcriptomic Atlas of Human Neocortical Development during Mid-gestation. *Neuron* **103**, 785–801.e8 (2019).

40. Langfelder, P. & Horvath, S. WGCNA: an R package for weighted correlation network analysis. *BMC Bioinformatics* **9**, 559 (2008).

41. Hawrylycz, M. *et al.* Canonical genetic signatures of the adult human brain. *Nat. Neurosci.* **18**, 1832–1844 (2015).

42. Hartl, C. L. *et al.* Coexpression network architecture reveals the brain-wide and multiregional basis of disease susceptibility. *Nat. Neurosci.* **24**, 1313–1323 (2021).

43. Yeo, B. T. T. *et al.* The organization of the human cerebral cortex estimated by intrinsic functional connectivity. *J. Neurophysiol.* **106**, 1125–1165 (2011).

44. Pfeifer, R. A. *Die angioarchitektonische areale gliederung der grosshirnrinde: auf grund vollkommener gefässinjektionspräparate vom gehirn des macacus rhesus*. (G. Thieme, 1940).

45. Palomero-Gallagher, N. & Zilles, K. Cortical layers: Cyto-, myelo-, receptor- and synaptic architecture in human cortical areas. *Neuroimage* **197**, 716–741 (2019).

46. Monier, A. *et al.* Entry and distribution of microglial cells in human embryonic and fetal cerebral cortex. *J. Neuropathol. Exp. Neurol.* **66**, 372–382 (2007).

47. Menassa, D. A. & Gomez-Nicola, D. Microglial Dynamics During Human Brain Development. *Front. Immunol.* **9**, 1014 (2018).

48. Molnár, Z. *et al.* New insights into the development of the human cerebral cortex. *J. Anat.* **235**, 432–451 (2019).

49. Collins, C. E., Airey, D. C., Young, N. A., Leitch, D. B. & Kaas, J. H. Neuron densities vary across and within cortical areas in primates. *Proceedings of the National Academy of Sciences* **107**, 15927–15932 (2010).

50. Spocter, M. A. *et al.* Neuropil distribution in the cerebral cortex differs between humans and chimpanzees. *J. Comp. Neurol.* **520**, 2917–2929 (2012).

51. Collins, C. E. *et al.* Cortical cell and neuron density estimates in one chimpanzee hemisphere. *Proc. Natl. Acad. Sci. U. S. A.* **113**, 740–745 (2016).

52. Nieuwenhuys, R. & Broere, C. A. J. A map of the human neocortex showing the estimated overall myelin content of the individual architectonic areas based on the studies of Adolf Hopf. *Brain Struct. Funct.* **222**, 465–480 (2017).

53. Haney, J. R. *et al.* Broad transcriptomic dysregulation across the cerebral cortex in ASD. *bioRxiv* 2020.12.17.423129 (2020) doi:10.1101/2020.12.17.423129.

54. Di Martino, A. *et al.* The autism brain imaging data exchange: towards a large-scale evaluation of the intrinsic brain architecture in autism. *Mol. Psychiatry* **19**, 659–667 (2013).

55. Di Martino, A. *et al.* Enhancing studies of the connectome in autism using the autism brain imaging data exchange II. *Sci Data* **4**, 170010 (2017).

56. Ruzzo, E. K. *et al.* Inherited and De Novo Genetic Risk for Autism Impacts Shared Networks. *Cell* **178**, 850–866.e26 (2019).

57. Satterstrom, F. K. *et al.* Large-Scale Exome Sequencing Study Implicates Both

Developmental and Functional Changes in the Neurobiology of Autism. *Cell* **180**, 568–584.e23 (2020).

58. Singh, T. *et al.* Exome sequencing identifies rare coding variants in 10 genes which confer substantial risk for schizophrenia. *medRxiv* 2020.09.18.20192815 (2020).
59. Deciphering Developmental Disorders Study. Prevalence and architecture of de novo mutations in developmental disorders. *Nature* **542**, 433–438 (2017).
60. Heyne, H. O. *et al.* De novo variants in neurodevelopmental disorders with epilepsy. *Nat. Genet.* **50**, 1048–1053 (2018).
61. Tam, V. *et al.* Benefits and limitations of genome-wide association studies. *Nature Reviews Genetics* vol. 20 467–484 (2019).
62. Kravitz, D. J., Saleem, K. S., Baker, C. I., Ungerleider, L. G. & Mishkin, M. The ventral visual pathway: an expanded neural framework for the processing of object quality. *Trends in Cognitive Sciences* vol. 17 26–49 (2013).
63. Parikshak, N. N. *et al.* Integrative functional genomic analyses implicate specific molecular pathways and circuits in autism. *Cell* **155**, 1008–1021 (2013).
64. Fischl, B. FreeSurfer. *Neuroimage* **62**, 774–781 (2012).
65. Rakic, P., Ayoub, A. E., Breunig, J. J. & Dominguez, M. H. Decision by division: making cortical maps. *Trends Neurosci.* **32**, 291–301 (2009).
66. Toro, R. & Burnod, Y. A Morphogenetic Model for the Development of Cortical Convolutions. *Cereb. Cortex* **15**, 1900–1913 (2005).
67. Ronan, L. *et al.* Differential tangential expansion as a mechanism for cortical gyrification. *Cereb. Cortex* **24**, 2219–2228 (2014).
68. Van Essen, D. C. A 2020 view of tension-based cortical morphogenesis. *Proc. Natl. Acad. Sci. U. S. A.* (2020) doi:10.1073/pnas.2016830117.
69. Smith, S. M. *et al.* An expanded set of genome-wide association studies of brain imaging

phenotypes in UK Biobank. *Nat. Neurosci.* **24**, 737–745 (2021).

Acknowledgements

The authors would like to thank all the participants and their families for their generous involvement in this study. A.R. was supported by the National Institute of Mental Health Intramural Research Program (NIH Annual Report Number, 1ZIAMH002949-04). K.S.W. was supported by the Wellcome Trust (215901/Z/19/Z). R.T.S. was partially supported by R01MH112847 and R01MH123550. S.N.V. was partially supported by R01MH123563. T.D.S. was supported in part by R01MH112847, R37MH125829, R01MH120482, and R01EB022573. R.D. was supported by the Gates Cambridge Trust. T.T.M. was supported by funds from NIH T32HG010464. P.E.V. is a Fellow of MQ: Transforming Mental Health (MQF17_24). J.S. was supported by NIMH T32MH019112-29 and K08MH120564. S.A. was supported by the Rosetrees Trust (A2665). A.A.B. was supported by NIH K08MH120564.

Competing interests

R.T.S. receives consulting income from Octave Bioscience and compensation for reviewership duties from the American Medical Association. All other authors declare no competing interests.

Author contributions

K.W., J.S., S.L. and A.R. conceived the project. K.W., S.A., J.S., S.V., T.M., R.D., A.R.D., T.S., S.L., P.E.V., R.T.S., A.A-B., D.H.G., and A.R., designed the experiments. K.W. and A.R. wrote the manuscript. All authors reviewed the manuscript.

Data availability

The cortical dense expression maps of 20,781 genes and ~30k vertices that support the findings of this study are available in link to MAGICC.

Methods

Methods overview:

1. Creating spatially dense maps of human cortical gene expression (Fig 1a-d)

Cortical surfaces were reconstructed for each AHBA donor MRI using FreeSurfer[1], and coregistered between donors using multimodal surface matching[2]. An average donor cortical mesh was also created for analyses of cortical morphology, by averaging the vertex coordinates of volumetrically aligned meshes for the 6 donors.

Probe-level data measures of gene expression for all samples in the AHBA adult brain microarray dataset were downloaded from (https://human.brain-map.org/static/download) - providing log2-transformed measures of gene expression for 58,692 probes in each of 3,702 brain tissue samples from six donors (**Table S1**). Within- and across-brain normalization of these probe level gene expression values was implemented as detailed by the Allen Institute for Brain Science White Paper (http://help.brain-map.org/download/attachments/2818165/WholeBrainMicroarray_WhitePaper.pdf). Probes were reannotated using the updated manifest from Arnautkevic et al[3], excluding genes lacking an Entrez, and probe-level expression values were averaged for each gene to yield a single gene*sample expression matrix for each donor. As only 2 donors had measurements from right hemispheres, samples were filtered by region to retain those originating from the cerebral cortex left hemisphere only. This decision was made given evidence for potential asymmetries in gene expression within the human cortex[4], and known differences in cortical shape between the hemispheres that complicate the reflection of sample locations from left to right cortical sheets[5]. The above steps resulted in a final set of 6 donor-level gene*sample matrices from the left cerebral cortex for downstream analyses. These matrices collectively contained scaled expression values for 20,781 genes in each of 1304 cortical samples.

Native subject MRI coordinates were extracted for every cortical sample in each donor (**Fig 1a**). Nearest mid-surface cortical vertices were identified for each sample, excluding samples further than 20mm from a cortical coordinate. For cortical vertices with no directly sampled expression, expression values were interpolated from their nearest sampled neighbor vertex[6] (**Fig 1b**). Sampling density ρ in each subject was calculated as the number of samples per mm^2, from which average inter-sample distance, *d,* was estimated using the formula: $d = \frac{1}{\sqrt{\rho}}$, giving a mean intersample distance of 17.7mm ± 1.2mm. Surface expression maps were smoothed with a 20mm full-width at half maximum Gaussian kernel, selected to be consistent with this sampling density (**Fig 1c**). To align subjects' expression, expression values were z-scored by the mean and standard deviation across vertices and then averaged across the 6 subjects (**Fig 1d**) - yielding spatially dense estimates of expression at 29696 vertices across the left cerebral cortex per gene. For Y-linked genes, DEMs were calculated from male donors only. For each of the resulting 20,781 gene-level expression maps, the orientation and magnitude of gene expression change at each vertex (i.e. the gradient) was calculated for folded, inflated and flattened representations of the cortical sheet.

2. Benchmarking dense expression maps (DEMs)

a. Replicability and independence from cortical sampling density (Fig S1).

We assessed the replicability of DEMs by applying the above steps for DEM generation to non-overlapping donor subsets and comparing DEMs between the resulting sub-atlases. We quantified DEM agreement between sub-atlases at both the gene-level (correlation in expression across vertices for each gene, **Fig 1c,d**) and the vertex-level (correlation in ranking of genes by their scaled expression values at each vertex, **Fig 1e,f**). These sub-atlas comparisons were done between all possible pairs of individuals, donor duos and donor triplets to give distributions and point estimates of reproducibility for atlases formed of 1, 2 and 3 donors. Learning curves were fitted to these data to estimate the projected gene-level and vertex-level DEM reproducibility of our full 6-subject sample atlas[7](**Fig S1c,e**).

To assess the effect of data interpolation in DEM generation we compared gene-level and vertex-level reproducibility of DEMs against a "ground truth" estimate of these reproducibility metrics based on uninterpolated expression data. To achieve a strict comparison of gene expression values between different individuals at identical spatial locations we focused these analyses on the subset of AHBA samples where samples from two subjects were within 3 mm geodesic distance of one another. This resulted in 582 instances (spatial locations) with measures of gene expression for pairs of donors from both DEMs and un-interpolated AHBA expression data. We computed gene-level and vertex-level reproducibility of expression using the paired donor data at each of these sample points - for both DEM and uninterpolated AHBA expression values. By comparing DEM reproducibility estimates with those for uninterpolated AHBA expression data, we were able to quantify the combined effect of interpolation and smoothing steps in DEM generation. We used cross-vertex correlation to compare vertex-level reproducibility values between DEMs and uninterpolated AHBA expression data (**Fig S1a**). We used gene-level reproducibility values from DEMs and uninterpolated AHBA expression data to compute a gene-level difference in reproducibility, and we then visualized the distribution of these difference values across genes (**Fig S1b**).

Theoretically, regional gradients of expression change in DEMs could be biased by regional variations in the density of AHBA cortical sampling. To test for this, in each individual subject, we calculated the spatial relationship between the sampling density and mean gene gradient magnitude (**Fig S1g**). We additionally tested whether the regional variability of gene rank predictability in the atlas (shown in **Fig S1h**) was linked to the sampling density within the atlas.

b. Alignment with reference measures of cortical organization (Fig 1 e-g)

We first determined if our DEM library was able to differentiate between genes that are known to show cortical expression (CExp) and those without any prior evidence of cortical expression (NCExp) - motivated by the strong expectation that NCExp genes should lack a consistent spatial gradient in expression. For this test, we defined a set of 16573 CExp genes by concatenating the genes coding for proteins found in the "cortex" tissue class of the human

protein atlas[8] genes identified as markers for cortical layers or cortical cells (see below,[9–19]). The remaining 4,208 genes in our DEM library were classified as NCExp. Independent T-tests were used to assess whether the distributions of gene-level reproducibility values differed significantly between CExp and NCExp genes (**Fig S1d**). We projected vertex-level reproducibility values for CExp and NCExp genes onto the cortical surface for visual comparison, and also computed the mean cross-vertex reproducibility for each of these maps (**Fig S1f**).

We next compiled data from independent studies for a range of macroscale and microscale cortical features that would be expected to align with specific DEM maps, and asked if the spatial patterns of cortical gene expression from DEMs showed the expected alignment with these independent data. These independent comparison studies were selected to span diverse measurement methods and data modalities representing a range of spatial scales. We benchmarked DEMs against orthogonal spatially dense measures of cortical through the following comparisons: (i) motor-associated areas of the cortex from multimodal in vivo MRI[20], vs. the average DEM for two marker genes (ASGR2, CSN1S1) of Betz cells, which are giant pyramidal neurons that output from layer V of the human motor cortex[21]; (ii) an in vivo neuroimaging map of the T1/T2 ratio measuring of intracortical myelination[22] vs. the DEM for Myelin Basic Protein; (iii) Layer IV thickness values from the 3D BigBrain atlas of cortical layers[23] vs. the average DEM for later IV marker genes[18,19] (**Table S2**); and, (iv) regional cortical thinning from in vivo sMRI data in Alzheimer disease patients with the APOE E4 (OASIS-3 dataset[24] , see ***MRI Data Processing*** below) vs. the APOE4 DEM. For all four of these comparisons, alignment between maps was quantified and test for statistical significance using a strict spin-based spatial permutation method that controls for spatial autocorrelation in cortical data ([25]methods on statistical testing of pairwise cortical maps can be found in the ***Statistical Methods Table below***).

We also sought to benchmark DEMs against regional differences in cellular measures of cortical organization from single nucleus RNA-sequencing studies (snRNA-seq). Specifically, we correlated regional differences in the estimated proportion of 16 neuronal subtypes across 6 cortical regions[9] with regional DEM estimates for the mean expression of provided markers for these cell types[9]. The test statistic was tested against a null distribution generated through spinning and resampling the cell marker DEM estimates (***Statistical Methods Table***). Given the observed correspondence between regional cellular proportions and regional expression of cell marker sets, we used more recently-generated reference cell-markers from the Allen Institute for Brain Sciences[11,21,26] to generate DEMs for 11 of 14 major cell subclasses in the mammalian cortex (6 neuronal types shown in **Fig 1g,** all 11 used for TD peak enrichment analysis **Fig S2e**). Three markers were excluded due to absence in the original dataset or low gene-predictability ($r<0.2$, **Fig S1d**).

3. Characterizing the topography of DEMs

a. Transcriptomic distinctiveness (TD) and principal component analysis (Fig 2a-c)

Transcriptomic distinctiveness (TD) of each cortical vertex was calculated as the mean of the absolute DEM value for all genes (**Fig 2a**). Statistically significant peaks in TD, driven by convergence of extreme values across multiple genes, were identified as follows. The DEM for each gene was independently spun and TD was recalculated at each vertex over 1000 sets of

gene-level DEM permutations [25]. The maximum vertex TD value for each permuted TD map was recorded and the 95th percentile value across the 1000 permutations was taken as a threshold value. This threshold represents the maximum TD one would expect in the absence of concentrated colocalisations of extreme expression signatures, and areas above this threshold were annotated as TD peaks. To disambiguate TD peaks that are spatially coalescent but potentially driven by extreme values of heterogeneous gene sets within different regions, we concatenated all suprathreshold TD vertices into a single vertex*gene matrix and vertices in this matrix were clustered based on their expression signatures.

Intervertex correlation of gene rankings were calculated and the matrix was clustered using a gaussian mixture model. Bayesian information criterion was used to identify the optimum number of clusters (k=6) from a range of 2-18. Labels were given to each of these TD peaks based on their intersection with a reference multimodal neuroimaging parcellation of the human cortex[20]. Each TD was given the label of the multimodal parcel that showed greatest overlap (**Fig 2b**).

The cortical regions defined by TD peaks were annotated according to their spatial overlap with the 24 cortical cell marker expression DEMs used in **Fig 1** (Lake et al. 2016; Hodge et al. 2019; Bakken et al. 2021). To establish that cell maps were aligned with TD peaks, we first tested whether the vertex with the highest DEM value for each cell map overlapped with a TD peak and compared the number of overlapping cells to a null distribution created through spinning the TD peaks independently 1000 times. We then identified the cell types whose expression most closely aligned with each TD peak, comparing mean TD expression with a null distribution generated through spinning the peaks 1000 times (**Fig S2e**). TD peaks were also annotated for their functional activations using the meta-analytic Neurosynth database (see **Map annotations** below).

Gene sets characterizing TD peaks were identified as follows. At the vertex with the highest TD value within a peak region, the 95th centile TD value across genes was selected as a threshold. Genes with z-scored expression values above this threshold or below its inverse were selected, allowing TD peaks to have asymmetric length gene lists for high and low-expressed genes (**Table S3**). These TD gene lists were submitted to a Gene Ontology (GO) enrichment analysis pipeline (see ***Gene-set based annotations*** below).

To contextualize the newly-described TD peaks using previously-reported principal components (PCs) of human cortical gene expression, we computed the first 5 PC of gene expression in our full DEM library. The percentage of variance explained by each PC was calculated and compared to a null threshold derived through fitting PCs to a permuted null given by 1000 random spatial rotations of gene-level DEMs (**Fig S2a**). Taking the gene-level loadings from the first 3 PCs (**Fig S2b**), each vertex could be positioned in a 3D PC space based on its expression signature and also be colored based on its membership of a TD peak - thereby visualizing the position of TD peaks relative to the dominant spatial gradients of transcriptomic variation across the cortex (**Fig 2c**).

The assignment of TD regions as "peaks" implies a rapid emergence of the TD signature surrounding the peak boundaries, which we formally assessed by cortex-wide analysis of local tangential changes in gene expression (see "***Local Gradient Analysis***" below), and a spatially fine-grained comparisons of the physical vs. transcriptional distance between cortical regions. In the

latter of these two analytic approaches, a rapid "border-like" onset of TD features would appear as (i) TD regions showing a greater transcriptional distance from other cortical regions than would be expected from their physical distance from other cortical regions, and (ii) this disparity emerging sharply surrounding the peak. To achieve this test, we first quantified the geodesic physical distance and Euclidean transcriptomic distance between pairs of vertices. For computational tractability, we limited this analysis to a subsample of vertices, choosing central vertices from ROIs in a parcellation with 500 approximately evenly sized parcels[27]. We fit a linear generalized additive model to the data - predicting transcriptomic distance from geodesic distance - and calculated the residuals for each inter-vertex edge (**Fig S2c**). For each sampled vertex we averaged these residuals and mapped them back to the surface to visualize cortical areas that were transcriptomically more distinctive than their physical distance to other areas would predict (**Fig S2d**).

b. Relating adult TD peaks to fetal gene expression (Fig S2g)

We sought to establish whether the regional expression signatures characterizing TD peaks were present early in fetal development. This goal required measures of gene expression from multiple regions across the fetal cortical sheet, which are provided by the Allen Institute from Brain Sciences fetal laser micro-dissection microarray dataset[28]. In each samples' fetal brain, this dataset represents approximately 25 cortical brain regions tangentially, and radially 7 transient fetal layers/compartments radially: Subpial granular zone (SG), marginal zone (MZ), outer and inner cortical plate (grouped together as CP), subplate zone (SP), intermediate zone (IZ), outer and inner subventricular zone (grouped together as SZ), and ventricular zone (VZ).

Probe-level data measures of gene expression for the two PCW21 donors in the AHBA fetal LMD microarray dataset were downloaded from (https://www.brainspan.org/static/download.html) - providing log2-transformed measures of gene expression for 58,692 probes in each of 536 tissue samples across both donors (**Table S1**). Preprocessing and normalization of these probe level gene expression values was implemented as detailed by the Allen Institute for Brain Science White Paper (https://help.brain-map.org/download/attachments/3506181/Prenatal_LMD_Microarray.pdf). Probe-level expression values were averaged for each gene to yield a single gene*sample expression matrix for each donor, which was filtered to include only cortical samples. Gene expression values were scaled across samples within each donor, and scaled gene expression values were compiled for the set of 235 cortical regions that was common to both donor datasets. We averaged scaled regional gene expression values between donors per gene, and filtered for genes in the fetal LDM dataset that were also represented in the adult DEM dataset - yielding a single final 20,476*235 gene-by-sample matrix of expression values for the human cortex at 21 PCW. This matrix was then used to test if each TD expression signature discovered in the adult DEM dataset (**Fig 2**, **Table 3**) was already present in similar cortical regions at 21 PCW.

The analysis of fetal regional patterning of TD peak gene sets was carried out as follows (**Fig S2g**). For a given TD peak, the significantly enriched genes for that peak (see above for definition of these gene sets) were identified in the fetal dataset and averaged at each fetal sample - capturing how highly expressed the TD signature was in each fetal sample. Next, we identified all samples in the fetal expression dataset that originated from regions underlying the

TD peak, and defined these as the "fetal target region set" for that TD region (i.e. occipital samples in the fetal brain were the fetal target region set for analysis of gene enriched in the adult occipital TD region). We ranked all fetal samples by their mean expression of the TD marker set, and normalized these ranks to between 0 (TD markers most highly expressed) and 1 (TD markers most lowly expressed). Normalization was done to adjust for varying numbers of areas recorded per compartment. This ranking enabled us to compute the median rank of the fetal target region set, and test if this was significantly lower compared to a null distribution of ranks from random reassignment of the fetal target region set labels across all fetal samples. Within this analytic framework, a statistically significant test means that the adult TD signature is significantly localized to homologous cortical regions at 21 PCW fetal life (**Fig S2g**). We repeated this procedure for each adult TD.

c. Local gradient analysis (Fig 2e-g)

Spatially dense expression maps enabled the calculation of a vector describing the first spatial derivative - i.e. the local gradient - of each gene's expression at each vertex. These vectors describe both the orientation and the magnitude of gene expression change. Averaging these gene-level magnitude estimates across genes provided a vertex-level summary map of the magnitude of local expression changes in our full DEM library (**Fig 2e**). Regions with a significantly high average expression gradient were identified using a similar spatial permutation procedure as described for the identification of TD peaks. Briefly, the DEM gradient map for each gene was independently spun and an average expression gradient magnitude was recalculated at each vertex over 1000 sets of these spatial permutations[25]. For each permutation we recorded the maximum vertex-level average expression gradient value, and the 95th percentile value of these maximums across the 1000 permutations was taken as a threshold value. Vertices with observed average expression gradient values above this threshold represented cortical regions of significantly rapid transcriptional change (**Fig S2f**).

The principal orientation of gene expression change at each vertex was calculated considering the vectors describing gene expression gradients - thereby providing a single summary of local gene expression gradients that considers both direction and magnitude. Principal component analysis (PCA) of gene gradient vectors was used to calculate the primary orientation of gene expression change at each vertex (**Fig 2e**) and the percentage of orientation variance accounted for by this principal component (**Fig 2e, Fig S2e**). Gene-level PC weights for each vertex were stored for subsequent analyses, including alignment with folds and functional ROIs (**Fig 2f & g**, see annotational analyses below).

The rich DEM expression gradient information described above was applied in three downstream analyses. First, we used these resources to detail the emergence of TD expression signatures within the cortical sheet - focusing on all vertices that had been identified to show a significantly elevated mean expression gradient. Specifically, we ranked genes at these vertices by their loadings onto the 1st PC of gene expression gradients at each vertex, and correlated these rankings with the rankings of genes by the expression at each TD peak vertex. This vertex-level correlation score - which quantifies how closely the gene expression gradient at a given vertex resembles that expression signature of a given TD peak - was regenerated for each of the

6 TD peaks (colors, **Fig S2f**). In each of these 6 maps, we were also able to plot the principal orientations of expression change at the vertex-level (red lines, **Fig S2f**) to ask if gradients of expression change for a given TD signature were spatially oriented towards the TD in question.

Second, we used the principal orientation of expression change at each vertex to assess whether local transcriptomic gradients were aligned with the orientation of cortical folding patterns. Orientation of cortical folds was calculated using sulcal depth and cortical curvature [29]. Gradient vectors for sulcal depth describe the primary orientation of cortical folds on the walls of sulci, while gradient vectors of cortical curvature better describe the orientation at sulcal fundi and gyral crowns. These two gradient vector-fields were combined and smoothed with a 10mm FWHM gaussian kernel to propagate the vector field into plateaus e.g. at large gyral crowns where neither sulcal depth nor curvature exhibit reliable gradients. The folding orientation vectors were calculated with reference to a 2D flattened cortical representation for statistical comparison with the gradient vectors derived from gene expression maps (**Fig 2f**). At each vertex, the minimum angle was calculated between the folding orientation vector and gene expression gradient vector. Aligned vector maps exhibit positive skew, with angles tending towards zero. Therefore the skewness of the distribution of angles across all vertices was calculated, and to test for significance, folding and expression vector maps were spun relative to one another 1000 times, generating a null distribution of skewness values against which the test-statistic was compared (**Statistical methods table**). A similar analysis was applied to test the association between module eigenmap gradient vectors and cortical folding (see ***WGCNA section*** below).

Third we sought to quantify the alignment between cortical expression gradients and cortical areas as defined by multimodal imaging. Orientation of each MRI multimodal parcel ROI from Glasser et al[20], was calculated taking the coordinates for all vertices within a given ROI. Principal Component Analysis of coordinates was used to identify the short and long axis of the ROI object. The vector describing the short axis was taken for comparison with mean of expression gradient vectors for vertices in the same ROI. For each ROI, the minimum angle was calculated and the skewness of the angles across all ROIs was calculated and compared to a null distribution created through spinning maps independently 1000 times, recalculating angles and their skewness (**Fig 2g**).

d. Weighted Gene Co-expression Network Analysis (WGCNA) (Fig 3a-c)

Genes were clustered into modules for further analysis using WGCNA[30]. Briefly, gene-gene cortical spatial correlations were calculated across all vertices to generate a single square 20,781*20,781 signed co-expression matrix. This co-expression matrix underwent “soft-thresholding”, raising the values to a soft power of 6, chosen as the smallest power where the resultant network satisfied the scale-free topology model fit of $r^2>0.8$[31]. Next, a similarity matrix was created through calculating pairwise topological overlap, assessing the extent to which genes share neighbors in the network[32]. The inverse of the topological overlap matrix was then clustered using average linkage hierarchical clustering, with a minimum cluster size of 30 genes. The eigengene for each module is the first principal component of gene expression across vertices, and provides a single measure of module expression at each vertex (hence, “eigenmap”). As per past implementation of WGCNA, pairs of modules with eigengene correlations above 0.9 were merged. These procedures defined a total of 23 gene co-expression

modules ranging in size from 77-3725 genes, and a single set of unconnected genes (gray module 265 genes). We filtered the gray module from further analysis, as well as all 6 other modules that were also statistically significantly enriched for NCExp genes (**Table S4**, Fisher's test, all p<0.0001) - leaving a total of 16 modules for downstream analysis (**Table S4**).

Each WGCNA module could be visualized as a cortical eigenmap, and eigenmap gradient - on the TD terrain, or inflated cortical (**Fig 3a**). The eigenmap gradient for each module provides a vertex-level measure for the magnitude of change in module expression at each vertex, as well as a vertex-level orientation of module expression change - calculated as described in ***Local Gradient Analysis*** above. These anatomical representations of each WGCNA module are amenable to spatial comparison with any other cortical map through spatial permutations[25] (see ***Annotational analyses*** below). Each WGCNA module is also defined as a gene set, which is amenable to standard gene-set based enrichment analysis (see ***Annotational analyses*** below). WGCNA modules can each also be represented as a ranked list of all genes - based on gene-level kME scores for each module, which are the cross-vertex correlation between a gene's DEM map and a module's eigenmap.

4. Multiscale annotation of WGCNA modules (Fig 3c,d)

We used multiple open neuroimaging and genomic datasets to systematically sample diverse levels of cortical organization and achieve a multiscale annotation of WGCNA modules. All gene sets used in enrichment analysis are detailed in **Table S2**.

a. Map-based annotations

MRI-derived maps of cortical function: Functional annotations of the cortex were carried out using two independent functional MRI (fMRI) resources - one based on resting state fMRI (rs-FMRI)[33], and one using task-based fMRI[34,35]. Resting state functional connectivity networks were taken from[33], which divides the cortex into seven coherent functional networks through surface-based clustering of resting state fMRI into: visual, somatomotor, dorsal attention, ventral attention, frontoparietal control, limbic and default networks. We used spin-based spatial permutation testing to test for networks in which WGCNA eigenmap expression was significantly elevated (**Fig 3c, see *Statistical Methods Table***).

For task fMRI-driven functional annotation of the cortex, we drew on meta-analytic maps of cortical activation from *Neurosynth*[34,35]. Briefly, over 11,000 functional neuroimaging studies were text-mined for papers containing specific terms and associated activation coordinates [34]. Secondary analyses generated activation maps for 30 topics spanning a range of cognitive domains [35]. Topic activation maps were intersected with cortical surface meshes and thresholded to identify vertices with an activation value above 0. Example topics included "motor, cortex, hand" and "social, reasoning, medial prefrontal cortex" (**Fig 3d**). Topics were excluded if intersected cortical maps indicated activation in fewer than 1% of cortical vertices. Topic maps were used to annotate TD peaks (**Fig 2d**) - identifying for each ROI, the 2 topics with the highest Dice overlap. Topic maps also served as an independent validation of selected WGCNA eigenmaps (**Fig 2d**, ***Statistical Methods Table***). Topic maps from *Neurosynth* were also used to provide an orthogonal validation of observed resting state network enrichments from Yeo et al

(**Fig 3c**) for M2 and M12: mean eigenmap expression for module M2 and M12 was calculated for *Neurosynth* topic maps and assessed for statistical significance using spin-based permutations (**Fig 3d**, ***Statistical Methods Table***).

MRI-derived maps of cortical structure: Cortical thickness and T1/T2 "myelin" maps were taken from the Human Connectome Project average[20]. Spatial correlations were calculated across all vertices with each WGCNA module eigenmap, and assessed for statistical significance using spin-based permutations (**Fig 3c, see *Statistical Methods Table***).

Orientation of cortical folds: We used the orientation of expression change at each vertex to assess whether local eigenmap gradients were aligned with the orientation of cortical folding patterns, mirroring the analysis described above (**Fig S3a,** see ***Local Gradient Analysis***).

Inter-eigenmap correlations: We tested the pairwise spatial correlation between pairs of module eigenmaps. Statistical significance was assessed using a null distribution of correlation matrices through independently spinning eigenmaps and recalculating correlations, and correcting for multiple comparisons (**Fig S3b,** see ***Statistical Methods Table***).

b. Gene-set based annotations

GO enrichment: Gene Ontology Enrichment Analysis (see ***Statistical Methods Table*** below) were carried out on gene sets of interest, testing for enrichment of Biological Processes and Cellular Compartment, using the GOATOOLS python package[36]. Where multiple gene lists were assessed simultaneously (e.g. for TD peak gene lists or WGCNA gene sets), correction for multiple comparisons was carried out by dividing the $p<0.05$ threshold for statistical significance by the number of tests (i.e. for 16 module $p<0.05/16$). To facilitate summary descriptions of multiple significant GO terms, terms were hierarchically clustered based on semantic similarity [37] and representative terms were selected based on biological specificity (i.e. depth within the gene ontology tree) and magnitude of the enrichment statistic (***Fig 3d, Table S2***).

Layer marker gene sets and in situ hybridisation validation: We sought to assess the extent to which convergent spatial patterns of gene expression indicate convergent laminar and cellular features. Marker genes for each cortical layer were defined as the union of layer-specific marker genes from two comprehensive transcriptomic studies of layer-dependent gene expression sampling prefrontal cortical regions[18,19]. He et al., took human cortical samples from the prefrontal cortex, corresponding to areas BA 9, 10 & 46. Samples were sectioned into cortical depths and underwent RNAseq to identify 4131 genes exhibiting layer-dependent expression. Maynard et al., took samples from the dorsolateral prefrontal cortex and carried out spatial snRNAseq to identify 3785 genes enriched in specific cortical layers. These independent resources were combined for laminar enrichment analyses (i.e. we took each layer's marker genes to be the union of layer genes defined in Maynard et al and He at al). WGCNA module genes were tested for laminar enrichment using Fisher's exact test, correcting for multiple comparisons (**Fig 3c**, see ***Statistical Methods Table***). Independent validation of laminar associations of candidate genes identified through the above marker lists were carried out using in situ hybridisation (ISH) data from the Allen Institute[38]. For selected modules, we identified the highest kME genes represented within the ISH dataset. For each of these genes, the highest quality sections were downloaded, and the cortical ribbon was manually segmented. Equivolumetric estimates of cortical depth were generated and profiles of depth-dependent

staining intensity were generated[39]. Accompanying approximate cytoarchitectonic layer thickness estimations were derived from BigBrain and used to describe the laminar location of ISH peaks[23] (***Fig 3d***).

Adult cortical cell type marker gene sets: Cell marker gene sets were compiled from multiple snRNAseq datasets, sampling a wide variety of cortical areas covering occipital, temporal, frontal, cingulate and parietal lobes[9–17]. To integrate across differing subcategories, cell subtype marker lists were grouped into the following cell classes according to their designated names: excitatory neurons, inhibitory neurons, oligodendrocytes, astrocyte, oligodendrocyte precursor cells, microglia and endothelial cells. Marker lists for each of these cell classes represented the union of all subtypes assigned to the category. Cells not fitting into these categorisations were excluded. WGCNA module genes were tested for cell class marker enrichment using Fisher's exact test, correcting for multiple comparisons (**Fig 3c**, see ***Statistical Methods*** Table).

Fetal cortical cell type marker gene sets: Fetal cell marker gene lists were taken from Polioudakis et al[40]. WGCNA module genes were tested for cell class marker enrichment using Fisher's exact test, correcting for multiple comparisons (**Fig 3c**, see ***Statistical Methods Table***).

Compartments and SynGO: Cellular compartment gene lists were taken from the COMPARTMENTS database[41], which identifies subcellular localisation of marker genes based on integrated information from the Human Protein Atlas, literature mining and GO annotations. Examples of cellular compartments include nucleus, plasma membrane and cytosol. An additional compartment list for neuronal synapse was generated by collapsing all genes in the manually curated SynGO dataset[42]. WGCNA module genes were tested for cell compartment gene set enrichment using Fisher's exact test, correcting for multiple comparisons (**Fig 3c**, see ***Statistical Methods*** Table).

PPI network: Protein-protein interactions were derived from the STRING database[43]. Physical direct and indirect protein-protein interactions were considered. We tested for enrichment of protein-protein interactions for proteins coded by genes within WGCNA modules. The median number of intramodular connections was compared to a null distribution of median modular connectivity derived from 10000 randomly resampled modules with the same number of genes. Gene resampling was restricted within deciles defined by the degree of protein-protein connectivity.

Developmental peak epoch: Peak developmental epochs for genes were extracted from[44]. Briefly, bulk transcriptomic expression values were measured from DLPFC samples across development (6 PCW to 20 years), fitting developmental trajectories to each gene. Genes were categorized according to developmental epoch in which their expression peaked. For descriptive purposes, epochs were renamed as 1: "early fetal" ["fetal", 8 postconception weeks (PCW) - 24 PCW], 2: late fetal transition ("perinatal", 24 PCW - 6 months postnatal) and 3: "postnatal" (>6 months). Genes associated with WGCNA modules were tested for enrichment correcting for multiple comparisons across 16 modules.

Developmental trajectories: Gene-specific developmental trajectories were generated for the cortical samples from[16]. Briefly, in this study bulk transcriptomic expression values were measured from brain tissue samples taken from individuals aged between 5 PCW and 64 years old. In our analysis, samples were filtered for cortical ROIs and restricted to post 10 PCW due to

lack of samples before this time-point. Ages were log transformed and Generalized Additive Models were fit to each gene to generate an estimated developmental trajectory. To compute trajectory correlations between genes, we first resampled expression trajectories at 20 equally spaced time points (in log time), and then z-normalized these values per gene (using the mean and standard deviation of each trajectory). We then calculated expression trajectory Pearson correlations between each pair of genes in this dataset, and used these to determine if the spatially co-expressed genes defining each WGCNA module also showed significant temporal co-expression. To achieve this test, we calculated the median temporal co-expression (correlation in expression trajectories) for each WGCNA module gene set, and compared this to null median co-expression values for 1000 randomly resampled gene sets matching module size. Mean trajectories of genes in each module were calculated to visualize the developmental expression pattern of each module (**Fig S3c**).

Fetal compartmental analysis: We used the 21 PCW fetal microarray data processed for analysis of TD peaks (see ***Relating adult TD peaks to fetal gene expression*** above, **Fig S2g**)[28], to generated marker gene sets for each of 7 transient fetal cortical compartments: subpial granular zone (SG), marginal zone (MZ), outer and inner cortical plate (grouped together as CP), subplate zone (SP), intermediate zone (IZ), outer and inner subventricular zone (grouped together as SZ), and ventricular zone (VZ). We collapsed 21 PCW cortical expression data into compartments by averaging expression values across cortical regions for each compartment because compartment differences are known to explain the bulk of variation in cortical expression within this dataset (24%[28]). The top 5% expressed genes for each of the 7 fetal compartments was taken as the compartment marker set and used for enrichment analysis of WGCNA modules with Fisher's exact test, correcting for multiple comparisons (see ***Statistical Methods*** Table, **Fig 3c**).

5. Combining gene-set based annotations of the cortical sheet (Fig 3e, Fig S3d)

Our observation that many WGCNA modules showed statistically-significant enrichment for diverse gene sets that could span different spatial scales (e.g. layers and organelles) or temporal epochs (e.g. fetal and adult cortical features) (**Fig 3c**) suggested a potential sharing of marker gene across these diverse sets. To test this idea, and characterize potential biological themes reflected by these shared marker genes, we carried out pairwise enrichment analyses between all annotational gene lists (**Fig 3e**). Gene lists used for enrichment analysis of WGCNA modules for cortical layers, adult cells, cellular compartments, fetal cells, developmental peak epochs and fetal compartments, were taken for further analysis. A genelist-genelist pairwise enrichment matrix was generated. p-values above 0.1 were set to 1, to limit their contribution and p-values were converted to -log10(p). To remove isolated gene lists, all lists were ranked by their degree (edges defined as $p<0.05$) and the bottom 10% were excluded from further analysis. The matrix, excluding WGCNA modules, underwent Louvain clustering[45], grouping together gene lists with similar properties. Clusters were assigned descriptive names according to their salient common features (e.g. Non-neuronal, Mature neuron, Mitotic, Myelin, Fetal GE) (**Fig S3d**). For visualization, the full matrix underwent UMAP embedding[46], a non-linear dimensionality reduction technique assigning 2D coordinates to each gene list (**Fig 3e**), coloring gene lists by their assigned cluster along with the top 20% of edges.

6. Disease enrichment and ASD-based analysis of WGCNA modules

The proposed analyses above link regionally patterned cortical gene expression with macroscale imaging maps of structure and function, and microscale gene sets exhibiting laminar, cellular, subcellular and developmental transcriptomic specificity. We sought to assess whether WGCNA module gene lists capturing shared spatial and temporal features were also enriched for genes implicated in atypical brain development. We included genes identified in exome sequencing studies in neurodevelopmental disorders: autism spectrum disorder[47,48] (ASD), schizophrenia[49] (SCZ), severe developmental disorders[50] (Deciphering Developmental Disorders study, DDD) and epilepsy[51]. WGCNA module gene sets were tested for enrichment of these genes using Fisher's test and corrected for multiple comparisons (***Statistical Methods*** below**, Fig 4a**). Two modules - M12 and M15 - showed enrichment for multiple disease sets, with the ASD gene set being unique for showing enrichment in both modules. We therefore focused downstream analysis on further characterizing the enrichment of ASD genes in M12 and M15, and testing if these enrichments could predict regional cortical changes in ASD.

a. Characterizing ASD gene enrichments in M12 and M15

kME analysis: To better characterize the spatially distinctive properties of genes within M12 and M15, we defined the union of genes in both modules and collated the WGCNA-defined kME scores for each gene to both M12 and M15. This provided a basis for plotting all genes by their relative membership to both modules to: quantify the proximity of each gene to each module; assess the discreteness of gene assignment to modules; and - for any provide a common space within which to project gene functions and associations with ASD (**Fig 4c**)

Enrichment of ASD-linked GO terms: Genes linked to two specific GO terms, "Neuronal communication" and "Gene expression regulation", enriched amongst risk genes for Autism Spectrum Disorder in[48], were separately tested for enrichment within M12 and M15 (**Fig 4d**), using a Fisher's exact test.

Developmental trajectories of disease-linked modules: To characterize the distinctive temporal trajectories of M12 & M15 (see **Fig 3c**), we took gene-level trajectories (see ***Developmental trajectories*** above) and calculated the mean gene-expression trajectory of genes in each module (**Fig 4e**).

Independent characterisation of ASD risk genes: To assess the extent to which modules M12 & M15 captured the underlying axes of spatial patterning across all 135 ASD risk genes, we took DEMs for all 135 risk genes and independently clustered them. Pairwise co-expression was calculated for all risk gene DEMs and the resultant matrix was clustered using Gaussian mixture modeling into two clusters, C1 and C2 (**Fig S4a**). kME values were calculated for each risk gene with all WGCNA modules and averaged within each cluster. For each cluster, we then identified the WGCNA module with the highest mean kME (**Fig S4b**)

b. Comparing M12 and M15 expression to regional changes of cortical gene expression in ASD (Fig 4f)

We mapped regional transcriptomic disruption in ASD measured from multiple cortical regions using RNA-seq data[52]. This study compared bulk transcriptomic expression in ASD and control samples across 11 cortical areas, quantifying the extent of transcriptomic disruption by identifying the number of significantly differentially expressed genes in each region. Cortical areas sampled in this study were mapped to their closest corresponding area in a multimodal MRI parcellation[20]. The mean expression of M12 & M15 eigenmaps was quantified in the same cortical areas (**Fig 4f**). The test statistic, correlating eigenmap expression with the number of differentially expressed genes, was tested against a null distribution generated through spinning and resampling the eigenmaps (see **Statistical Methods Table**).

c. Comparing M12 and M15 expression to regional changes of cortical thickness in ASD (Fig 4g, h, Fig S4c)

To assess the extent to which WGCNA module eigenmaps pattern macroscale *in vivo* anatomical differences in ASD, we took the map of relative cortical thickness change in autism (see ***Preprocessing and analysis of structural MRI data*** below) and compared this to eigenmap expression patterns. M12 and M15 eigenmaps were thresholded, identifying the 5% of vertices with the highest expression. Areas of high significant thickness change were tested for overlap with areas of significant cortical thickness change using the Dice overlap compared to a null distribution of Dice scores generated through spinning the thresholded eigenmaps (see **Statistical Methods Table**)

7. Preprocessing and analysis of structural MRI data

a. AHBA donors

Pial and white matter cortical T1 MRI scans of the 6 AHBA donor brains were reconstructed using Freesurfer (v5.3)[53](see **Table S1**). Briefly, scans undergo tissue segmentation, cortical white and pial surface extraction. A mid-thickness surface, between pial and white surfaces was also created. The locations of tissue samples taken for bulk transcriptomic profiling, provided in the coordinates of the subject's MRI were mapped to the mid-thickness surface as outlined above (see **Creating spatially dense maps of human cortical gene expression from the AHBA**). Individual subject cortical surfaces were co-registered to the fs_LR32k template surface brain using MSMSulc[2] as part of the ciftify pipeline[54], which warps subject meshes by non-linear alignment their folding patterns to the MRI-derived template surface. A donor-specific template surface was created through averaging the coordinates of the aligned meshes and used for analysis of cortical folding patterns used in **Alignment with reference measures of cortical organization.** Pial, Inflated and flattened representations of the fs_LR32k surface were used for the visualization of cortical maps throughout.

b. OASIS (Fig 1e)

To estimate relative cortical thickness change in AD patients with the APOE E4 variant, we utilized the openly available OASIS database[24]**.** T1w MRI data collected using a Siemens Tim Trio 3T scanner and underwent cortical surface reconstruction using Freesurfer v5.3 as above.

Reconstructions underwent manual quality control and correction, with poor quality data being removed. Output cortical thickness maps, smoothed at 20mm fwhm and aligned to the fsaverage template surface were downloaded via https://www.oasis-brains.org/, along with age, sex, APOE genotype and cognitive status. Subjects were included in the analysis if they had been diagnosed with AD and had at least one APOE E4 allele (n=119), or were a healthy control (n=633) (see **Table S1**). Per-vertex coefficients for disease-associated cortical thinning and significance were calculated, adjusting for age, sex and mean cortical thickness. We controlled for mean CT to identify local anatomical changes given our finding of generalized cortical thickening in AD as compared to controls in OASIS. The map of cortical thickness coefficients was then registered from fsaverage to fs_LR32k for comparison with the DEM of APOE (**Fig 1e**)[2].

c. ABIDE

To estimate relative cortical thickness change in ASD, MRI cortical thickness maps, generated through Freesurfer processing of 3T T1 structural MRI scans were downloaded from ABIDE, along with age, sex, site information[55,56](**Table S1**). Multiple sites and scanners were used to acquire these data, which is known to introduce systematic biases in morphological measurements like cortical thickness. To mitigate this, we used neuroCombat which estimates and removes unwanted scanner-effects while retaining biological effects on variables such as age, sex and diagnosis[57]. Subjects with poor quality freesurfer segmentations were excluded using a threshold Euler count of 100 (ref). Cortical thickness change in ASD relative to controls was calculated adjusting for age, sex and mean cortical thickness. Neighbor-connected vertices exhibiting significant cortical thickness change ($p<0.05$) were grouped into clusters. A null distribution of cluster sizes was generated using 1000 random permutations of the cohort, storing the maximum significant cluster size for each permutation. The 95th percentile cluster size was used as a threshold for removing test clusters that could have arisen by chance[58]. Output coefficient and cluster maps were registered from fsaverage to fs_LR32k and compared with the M12 and M15 eigenmaps as described above

.

8. Statistical methods table

Statistical tests used to compare spatial maps and gene sets derived from the Allen Human Brain Atlas with independent multiscale neuroscientific resources.

Input data	**Test statistic**	**Significance test**
Comparison of two cortical maps e.g. Fig 1e	Pearson's R (e.g. Fig 1e,f), Spearman R_{rank} (Fig 3), delta Z for binary and continuous comparison (Fig 1e, Fig 3c & d), Dice score for two binary maps (Fig 2d, Fig 4g) skew in distribution of angles (Fig 2f & g, 3c). Counts for peak	Spin test: Generate null distribution for test statistic by independently spinning spherical projections of spatial maps and recalculating test statistic on spun maps[25]

	expression locations overlapping ROIs (Fig S2e).	
Intrasubject alignment of multimodal maps	Pearson's R (e.g. Fig S1h)	Simple permutation-based intermodal correspondence (SPICE) test[59]
Comparison of gene-gene connectivity matrix e.g. PPI vs spatial correlation, gene-gene spatial correlation vs developmental trajectory correlation	If continuous, threshold matrix at 95%. Fisher's exact test for significant edge-level overlap	Fisher's exact test p-values corrected for multiple comparisons using the Holm-Sidak step down procedure[60]
Overlap of two gene lists e.g. Fig 3e	Fisher's exact test	Fisher's exact p-value corrected for multiple comparisons
Cortical thickness changes in pathology (in AD Fig 1e, in ASD Fig 5e)	Linear model: Vertex cortical thickness ~ Age + sex + group + mean cortical thickness	Cluster-wise correction. Calculate maximum size of significant clusters on 1000 randomly permuted cohorts, using the 95th centile size as a threshold on the test cohort[58]
Intramodular trajectory correlation	Pairwise intramodular median rank correlation.	Randomly sampled gene sets of comparable size
Protein-protein interaction	Intramodular connectivity	Random resampling of gene sets with decile-matching for degree

1. Fischl, B. FreeSurfer. *Neuroimage* **62**, 774–781 (2012).

2. Robinson, E. C. *et al.* Multimodal surface matching with higher-order smoothness constraints. *Neuroimage* **167**, 453–465 (2018).

3. Arnatkeviciute, A., Fulcher, B. D. & Fornito, A. A practical guide to linking brain-wide gene expression and neuroimaging data. *Neuroimage* **189**, 353–367 (2019).

4. de Kovel, C. G. F., Lisgo, S. N., Fisher, S. E. & Francks, C. Subtle left-right asymmetry of gene expression profiles in embryonic and foetal human brains. *Sci. Rep.* **8**, 12606 (2018).

5. Jo, H. J., Saad, Z. S., Gotts, S. J., Martin, A. & Cox, R. W. Quantifying agreement between anatomical and functional interhemispheric correspondences in the resting brain. *PLoS One* **7**, e48847 (2012).

6. Moresi, L. & Mather, B. Stripy: A Python module for (constrained) triangulation in Cartesian coordinates and on a sphere. *J. Open Source Softw.* **4**, 1410 (2019).

7. Figueroa, R. L., Zeng-Treitler, Q., Kandula, S. & Ngo, L. H. Predicting sample size required for classification performance. *BMC Med. Inform. Decis. Mak.* **12**, 8 (2012).

8. Sjöstedt, E. *et al.* An atlas of the protein-coding genes in the human, pig, and mouse brain. *Science* **367**, (2020).

9. Lake, B. B. *et al.* Neuronal subtypes and diversity revealed by single-nucleus RNA sequencing of the human brain. *Science* **352**, 1586–1590 (2016).

10. Lake, B. B. *et al.* Integrative single-cell analysis of transcriptional and epigenetic states in the human adult brain. *Nat. Biotechnol.* **36**, 70–80 (2018).

11. Hodge, R. D. *et al.* Conserved cell types with divergent features in human versus mouse cortex. *Nature* **573**, 61–68 (2019).

12. Ruzicka, B. *et al.* Single-Cell Dissection of Schizophrenia Reveals Neurodevelopmental-Synaptic Link and Transcriptional Resilience Associated Cellular State. *Biol. Psychiatry* **89**, S106 (2021).

13. Velmeshev, D. *et al.* Single-cell genomics identifies cell type-specific molecular changes in autism. *Science* **364**, 685–689 (2019).

14. Habib, N. *et al.* Massively parallel single-nucleus RNA-seq with DroNc-seq. *Nat. Methods* **14**, 955–958 (2017).

15. Darmanis, S. *et al.* A survey of human brain transcriptome diversity at the single cell level. *Proc. Natl. Acad. Sci. U. S. A.* **112**, 7285–7290 (2015).

16. Li, M. *et al.* Integrative functional genomic analysis of human brain development and neuropsychiatric risks. *Science* **362**, (2018).

17. Zhang, Y. *et al.* Purification and Characterization of Progenitor and Mature Human Astrocytes Reveals Transcriptional and Functional Differences with Mouse. *Neuron* **89**, 37–53 (2016).

18. Maynard, K. R. *et al.* Transcriptome-scale spatial gene expression in the human dorsolateral prefrontal cortex. *Nat. Neurosci.* **24**, 425–436 (2021).

19. He, Z. *et al.* Comprehensive transcriptome analysis of neocortical layers in humans, chimpanzees and macaques. *Nat. Neurosci.* **20**, 886–895 (2017).

20. Glasser, M. F. *et al.* A multi-modal parcellation of human cerebral cortex. *Nature* **536**, 171–178 (2016).

21. Bakken, T. E. *et al.* Comparative cellular analysis of motor cortex in human, marmoset and mouse. *Nature* **598**, 111–119 (2021).

22. Glasser, M. F. & Van Essen, D. C. Mapping human cortical areas in vivo based on myelin content as revealed by T1- and T2-weighted MRI. *J. Neurosci.* **31**, 11597–11616 (2011).

23. Wagstyl, K. *et al.* BigBrain 3D atlas of cortical layers: Cortical and laminar thickness gradients diverge in sensory and motor cortices. *PLoS Biol.* **18**, e3000678 (2020).

24. LaMontagne, P. J. *et al.* OASIS-3: Longitudinal neuroimaging, clinical, and cognitive dataset for normal aging and Alzheimer disease. *bioRxiv* (2019) doi:10.1101/2019.12.13.19014902.

25. Alexander-Bloch, A. F. *et al.* On testing for spatial correspondence between maps of human brain structure and function. *Neuroimage* **178**, 540–551 (2018).

26. Tasic, B. *et al.* Adult mouse cortical cell taxonomy revealed by single cell transcriptomics. *Nat. Neurosci.* **19**, 335–346 (2016).

27. Schaefer, A. *et al.* Local-Global Parcellation of the Human Cerebral Cortex from Intrinsic Functional Connectivity MRI. *Cereb. Cortex* **28**, 3095–3114 (2018).

28. Miller, J. A. *et al.* Transcriptional landscape of the prenatal human brain. *Nature* **508**, 199–206 (2014).

29. Xia, J. *et al.* A COMPUTATIONAL METHOD FOR LONGITUDINAL MAPPING OF ORIENTATION-SPECIFIC EXPANSION OF CORTICAL SURFACE AREA IN INFANTS. *Proc. IEEE Int. Symp. Biomed. Imaging* **2018**, 683–686 (2018).

30. Langfelder, P. & Horvath, S. WGCNA: an R package for weighted correlation network analysis. *BMC Bioinformatics* **9**, 559 (2008).

31. Zhang, B. & Horvath, S. A general framework for weighted gene co-expression network analysis. *Stat. Appl. Genet. Mol. Biol.* **4**, Article17 (2005).

32. Yip, A. M. & Horvath, S. Gene network interconnectedness and the generalized topological overlap measure. *BMC Bioinformatics* **8**, 22 (2007).

33. Yeo, B. T. T. *et al.* The organization of the human cerebral cortex estimated by intrinsic functional connectivity. *J. Neurophysiol.* **106**, 1125–1165 (2011).

34. Yarkoni, T., Poldrack, R. A., Nichols, T. E., Van Essen, D. C. & Wager, T. D. Large-scale automated synthesis of human functional neuroimaging data. *Nat. Methods* **8**, 665–670 (2011).

35. Rubin, T. N. *et al.* Decoding brain activity using a large-scale probabilistic functional-anatomical atlas of human cognition. *PLoS Comput. Biol.* **13**, e1005649 (2017).

36. Klopfenstein, D. V. *et al.* GOATOOLS: A Python library for Gene Ontology analyses. *Sci. Rep.* **8**, 10872 (2018).

37. Resnik, P. Using Information Content to Evaluate Semantic Similarity in a Taxonomy. *arXiv [cmp-lg]* (1995).

38. Zeng, H. *et al.* Large-scale cellular-resolution gene profiling in human neocortex reveals species-specific molecular signatures. *Cell* **149**, 483–496 (2012).

39. Huber, L. (renzo) *et al.* LayNii: A software suite for layer-fMRI. *Neuroimage* **237**, 118091 (2021).

40. Polioudakis, D. *et al.* A Single-Cell Transcriptomic Atlas of Human Neocortical Development during Mid-gestation. *Neuron* **103**, 785–801.e8 (2019).

41. Binder, J. X. *et al.* COMPARTMENTS: unification and visualization of protein subcellular localization evidence. *Database* **2014**, bau012 (2014).

42. Koopmans, F. *et al.* SynGO: An Evidence-Based, Expert-Curated Knowledge Base for the Synapse. *Neuron* **103**, 217–234.e4 (2019).

43. Szklarczyk, D. *et al.* STRING v11: protein-protein association networks with

increased coverage, supporting functional discovery in genome-wide experimental datasets. *Nucleic Acids Res.* **47**, D607–D613 (2019).

44. Werling, D. M. *et al.* Whole-Genome and RNA Sequencing Reveal Variation and Transcriptomic Coordination in the Developing Human Prefrontal Cortex. *Cell Rep.* **31**, 107489 (2020).

45. Blondel, V. D., Guillaume, J.-L., Lambiotte, R. & Lefebvre, E. Fast unfolding of communities in large networks. *arXiv [physics.soc-ph]* (2008).

46. McInnes, L., Healy, J. & Melville, J. UMAP: Uniform Manifold Approximation and Projection for Dimension Reduction. *arXiv [stat.ML]* (2018).

47. Ruzzo, E. K. *et al.* Inherited and De Novo Genetic Risk for Autism Impacts Shared Networks. *Cell* **178**, 850–866.e26 (2019).

48. Satterstrom, F. K. *et al.* Large-Scale Exome Sequencing Study Implicates Both Developmental and Functional Changes in the Neurobiology of Autism. *Cell* **180**, 568–584.e23 (2020).

49. Singh, T. *et al.* Exome sequencing identifies rare coding variants in 10 genes which confer substantial risk for schizophrenia. *medRxiv* 2020.09.18.20192815 (2020).

50. Deciphering Developmental Disorders Study. Prevalence and architecture of de novo mutations in developmental disorders. *Nature* **542**, 433–438 (2017).

51. Heyne, H. O. *et al.* De novo variants in neurodevelopmental disorders with epilepsy. *Nat. Genet.* **50**, 1048–1053 (2018).

52. Haney, J. R. *et al.* Broad transcriptomic dysregulation across the cerebral cortex in ASD. *Cold Spring Harbor Laboratory* 2020.12.17.423129 (2020)

doi:10.1101/2020.12.17.423129.

53. Romero-Garcia, R. *et al.* Structural covariance networks are coupled to expression of genes enriched in supragranular layers of the human cortex. *Neuroimage* **171**, 256–267 (2018).

54. Dickie, E. W. *et al.* Ciftify: A framework for surface-based analysis of legacy MR acquisitions. *Neuroimage* **197**, 818–826 (2019).

55. Di Martino, A. *et al.* The autism brain imaging data exchange: towards a large-scale evaluation of the intrinsic brain architecture in autism. *Mol. Psychiatry* **19**, 659–667 (2013).

56. Di Martino, A. *et al.* Enhancing studies of the connectome in autism using the autism brain imaging data exchange II. *Sci Data* **4**, 170010 (2017).

57. Fortin, J.-P. *et al.* Harmonization of cortical thickness measurements across scanners and sites. *Neuroimage* **167**, 104–120 (2018).

58. Hagler, D. J., Jr, Saygin, A. P. & Sereno, M. I. Smoothing and cluster thresholding for cortical surface-based group analysis of fMRI data. *Neuroimage* **33**, 1093–1103 (2006).

59. Weinstein, S. M. *et al.* A simple permutation-based test of intermodal correspondence. *Hum. Brain Mapp.* **42**, 5175–5187 (2021).

60. Holm, S. A Simple Sequentially Rejective Multiple Test Procedure. *Scand. Stat. Theory Appl.* **6**, 65–70 (1979).